Ain Shams Engineering Journal (2015) 6, 1009–1030

Ain Shams University

Ain Shams Engineering Journal

www.elsevier.com/locate/asej
www.sciencedirect.com

Thermal radiation and heat generation/absorption effects on viscoelastic double-diffusive convection from an isothermal sphere in porous media

S. Abdul Gaffar [a], V. Ramachandra Prasad [b,*], E. Keshava Reddy [c], O. Anwar Bég [d]

[a] Department of Mathematics, Salalah College of Technology, Salalah, Oman
[b] Department of Mathematics, Madanapalle Institute of Technology and Science, Madanapalle 517325, India
[c] Department of Mathematics, Jawaharlal Nehru Technological University Anantapuramu, Anantapuramu 515002, India
[d] Gort Engovation Research (CFD), 15 Southmere Avenue, Great Horton, Bradford BD7 3NU, West Yorkshire, UK

Received 21 June 2014; revised 9 February 2015; accepted 27 February 2015
Available online 19 May 2015

KEYWORDS

Non-Newtonian Jeffreys fluid;
Rosseland thermal radiation model;
Isothermal sphere;
Keller-box numerical method;
non-Darcy flow;
Porous media

Abstract Buoyancy-driven convective heat and mass transfer in boundary layer flow of a viscoelastic Jeffrey fluid from a permeable isothermal sphere embedded in a porous medium is studied. Thermal radiation flux and heat generation/absorption are also incorporated in the model. A non-Darcy drag force model is employed to simulate the effects of linear porous media drag and second order Forchheimer drag. The Rosseland diffusion algebraic approximation is utilized to simulate thermal radiation effects. The non-dimensionalized boundary layer equations are solved using implicit, finite-difference scheme. The influence of Darcy number (Da), Deborah number (De), ratio of relaxation to retardation times (λ), radiation parameter (F), Forchheimer inertial parameter (Λ) and heat generation/absorption parameter (Δ), on normalized velocity, temperature, concentration, skin friction, heat and mass transfer rates are also studied. The present study has applications in the storage of nuclear waste materials.

1. Introduction

Heat and mass transfer in porous media arise in an extensive array of applications in modern nuclear engineering, mineral and chemical process engineering. These include transport of nuclear waste in geomaterial repositories [1–3], petroleum product filtration [4] and insulation systems [5]. The *non-Newtonian* nature of waste products has been identified by various studies [6]. Simulations of non-Newtonian transport in porous media have therefore employed a diverse range of rheological models

* Corresponding author. Tel.: +91 9160020785.
E-mail addresses: abdulsgaffar143@gmail.com (S. Abdul Gaffar), rcpmaths@gmail.com (V. Ramachandra Prasad), eddulakr@gmail.com (E. Keshava Reddy), o.beg@shu.ac.uk (O. Anwar Bég).
Peer review under responsibility of Ain Shams University.

Production and hosting by Elsevier

http://dx.doi.org/10.1016/j.asej.2015.02.014

Nomenclature

a	radius of the sphere
C	concentration
C_f	skin friction coefficient
c_p	specific heat parameter
Da	Darcy parameter
De	Deborah number
D_m	mass (species) diffusivity
F	radiation parameter
f	non-dimensional steam function
Gr	Grashof number
g	acceleration due to gravity
K	thermal diffusivity
k	thermal conductivity of Jeffreys fluid
k^*	the mean absorption coefficient
N	Buoyancy ration parameter
Nu	local Nusselt number
Pr	Prandtl number
q_r	radiative heat flux
$r(x)$	radial distance from symmetrical axis to surface of the sphere
Sc	Schmidt number
Sh	local Sherwood number
$\boldsymbol{S}$	extra stress tensor
T	temperature of the Jeffreys fluid
$\boldsymbol{T}$	Cauchy stress tensor
u, v	non-dimensional velocity components along the x- and y-directions, respectively
V	velocity vector
x	stream wise coordinate
y	transverse coordinate

Greek symbols

α	thermal diffusivity
β	the coefficient of thermal expansion
β^*	the coefficient of concentration expansion
λ	ratio of relaxation to retardation times
λ_1	retardation time
ϕ	non-dimensional concentration
Γ	inertial drag coefficient
Λ	the local inertial drag coefficient (Forchheimer parameter)
Δ	heat generation (source)/heat absorption (sink) parameter
η	the dimensionless radial coordinate
μ	dynamic viscosity
ν	kinematic viscosity
θ	non-dimensional temperature
ρ	density of non-Newtonian fluid
σ^*	the Stefan–Boltzmann constant
ξ	the dimensionless tangential coordinate
ψ	dimensionless stream function

Subscripts

w	conditions on the wall (sphere surface)
∞	free stream conditions

including Bingham plastic models [7], capillary hybrid viscoelastic models incorporating a viscous mode and an elongational mode [8], viscoplastic Schwedoff–Bingham fluids [9], Maxwell fluids [10], power-law fluids [11] and pseudoplastic fluids [12], Stokesian couple stress fluids [13] and Reiner–Rivlin third grade differential liquids [14]. These studies have adopted a variety of simulation approaches for porous media including percolation theory [9], volume-averaging [10] and network modelling [12]. They have generally employed the *Darcy model* which is valid for viscous-dominated low Reynolds number transport. Kadet and Polonski [9] however also considered inertial (Forchheimer) losses for higher Reynolds numbers. Non-Darcian flows may involve Forchheimer effects and also Brinkman vorticity diffusion effects, channeling, tortuosity and other phenomena. Vafai [15] presented a seminal theoretical and experimental study of the influence of variable porosity and also inertial forces (Forchheimer drag) on thermal convection flow in porous media, with the channelling effect being studied in detail. He elucidated the qualitative aspects of variable porosity in generating the channelling effect with an asymptotic analysis. A number of investigations have subsequently addressed rheological flows in non-Darcian porous media. Anwar Bég et al. [16] used a finite element method to simulate micropolar heat and mass transfer in Darcy–Forchheimer porous media with cross-diffusion effects. Kairi and Murthy [17] analyzed the influence of melting and Soret diffusion on mixed convection heat and mass transfer from vertical surface adjacent to an Ostwald–de Waele power law fluid-saturated non-Darcy porous medium. Anwar Bég et al. [18] used an electrical thermal network solver code (**PSPICE**) to simulate the magnetohydrodynamic heat transfer in Walter-B viscoelastic flow in Darcy–Forchheimer porous media. Prasad et al. [19] studied the non-Darcy effects on thermal convection boundary layer flow of a second order Reiner–Rivlin fluid in a porous medium. Rashidi et al. [20] used a differential transform numerical solver to study Forchheimer drag and buoyancy effects on magneto-micropolar thermal convection in a vertical porous medium conduit.

In many chemical engineering and nuclear process systems, *curved bodies* are also encountered. These include cylinders, cones, ellipses and spherical geometries. Several studies have considered heat and/or mass transfer from curved bodies to non-Newtonian fluids. An early investigation was presented by Bhatnagar [21] who considered analytically the thermal convection from a rotating and thermally insulated spherical body to a viscoelastic Reiner–Ericksen fluid as a simulation of polysiloxane polymer performance. He identified that secondary flow degenerates into two distinct zones and that thermal convection dominates over dissipation effects due to the influence of viscoelasticity. Lee and Donatelli [22] studied species diffusion in power-law fluid flow from a sphere. Nazar et al. [23] analyzed numerically the natural convection of micropolar fluid from a horizontal cylindrical geometry. Dhole et al. [24] used a finite volume computational code to examine the influence of Reynolds number, Prandtl number and rheological power law index (n) on the heat-transfer from

an unconfined sphere submerged in an isothermal and incompressible power law fluid, under both isothermal and isoflux thermal boundary conditions on the sphere surface. Very recently Prasad et al. [25] used a finite difference method to study natural convection boundary layer flow of a Casson non-Newtonian fluid from a permeable horizontal cylinder with thermal and hydrodynamic slip, showing that an increase in Casson rheological parameter acts to elevate considerably the skin friction but depresses temperatures. Anwar Bég et al. [26] investigated numerically thermo-diffusion and diffuso-thermal effects on double-diffusive natural convection from a spherical body to a micropolar rheological fluid. Akbar et al. [27] investigated the combined effects of slip and convective boundary conditions on stagnation-point flow of CNT suspended nanofluid over a stretching sheet.

Thermal radiation effects also arise in nuclear engineering applications including reactors, propulsion systems, etc. When coupled with thermal convection flows, these transport phenomena problems are highly nonlinear. At a high temperature the presence of thermal radiation changes the distribution of temperature in the boundary layer, which in turn affects the heat transfer at the wall. A variety of radiative heat transfer models have been utilized by thermal engineers for transport modelling in porous media. Rudraiah and Sasikumar [28] used the Milne–Eddington approximation and a Galerkin algorithm to simulate the stability of flow with conduction, convection and radiation heat transfer in a gray fluid-saturated sparsely packed non-Darcy porous medium. They observed that the nature of the bounding surfaces and thermal radiation flux have a strong influence on the critical Rayleigh and wave numbers. Talukdar et al. [29] employed the Chandrasekhar discrete transfer method (DTM) to simulate radiative-convective flow in a porous medium channel. Yih [30] used the Rosseland diffusion flux approximation to analyze computationally mixed convective-radiative flow from a wedge geometry embedded in a non-Darcian porous medium. Takhar et al. [31] used the Cogley–Vincenti–Giles differential flux model to study radiative-convective boundary layer flow in a Darcy–Forchheimer porous regime with a numerical code.

In the current article we investigate numerically the steady-state, boundary layer radiative-convective flow of a Jeffrey's viscoelastic fluid from a sphere immersed in a saturated non-Darcy porous medium. The transformed nonlinear boundary value problem is solved with the Keller-box finite difference method. A parametric study of the effect of the emerging thermophysical parameters i.e. *Darcy number (Da), Deborah number (De), ratio of relaxation to retardation times* (λ), *radiation parameter (F), Forchheimer inertial parameter* (Λ) *and heat generation/absorption parameter* (Δ), on normalized velocity, temperature, concentration, local skin friction, surface heat transfer rate (local Nusselt number) and surface mass transfer rate (local Sherwood number) is conducted. The present problem has to the authors' knowledge not appeared thus far in the scientific literature and is relevant to nuclear waste simulations and also polymeric processing.

2. Non-Newtonian constitutive Jeffreys fluid model

In the present study a subclass of non-Newtonian viscoelastic fluids known as the *Jeffreys fluid* [32–36] is employed owing to its simplicity. This fluid model is capable of describing the characteristics of relaxation and retardation times which arise in complex polymeric flows and also in liquids employed in geological nuclear waste repositories [37]. Furthermore the Jeffrey type model utilizes time derivatives rather than convected derivatives, which greatly facilitates numerical simulations. The Cauchy stress tensor, $\boldsymbol{T}$, of a Jeffrey's non-Newtonian fluid [38] takes the form as follows:

$$\boldsymbol{T} = -p\boldsymbol{I} + \boldsymbol{S}, \quad \boldsymbol{S} = \frac{\mu}{1+\lambda}(\dot{\gamma} + \lambda_1 \ddot{\gamma}) \tag{1}$$

where $\boldsymbol{S}$ is the extra stress tensor, a dot above a quantity denotes the material time derivative, p is pressure, $\boldsymbol{I}$ is the identity tensor, μ is dynamic viscosity, λ is the ratio of relaxation to retardation times, λ_1 is the retardation time and $\dot{\gamma}$ is the shear rate. The Jeffreys model provides an elegant formulation for simulating retardation and relaxation effects arising in non-Newtonian flows. The shear rate and gradient of shear rate are further defined in terms of velocity vector, $\boldsymbol{V}$, as follows:

$$\dot{\gamma} = \nabla \boldsymbol{V} + (\nabla \boldsymbol{V})^T \tag{2}$$

$$\ddot{\gamma} = \frac{d}{dt}(\dot{\gamma}) \tag{3}$$

The introduction of the appropriate terms into the flow model is considered next. The resulting boundary value problem is found to be well-posed and permits an excellent mechanism for the assessment of rheological characteristics on the flow behaviour.

3. Mathematical flow model

Steady, double-diffusive, laminar flow of an optically-thick Jeffreys fluid from a permeable sphere embedded in an isotropic, homogenous, fully-saturated porous medium in the presence of a heat source/sink and appreciable thermal radiation heat transfer, is considered, as illustrated in Fig. 1. Thermal dispersion, viscous heating and stratification effects are neglected as are cross-diffusion effects. A non-Darcy drag force model is employed to simulate porous media bulk impedance and also inertial effects, following Anwar Bég et al. [18]. The x-coordinate is measured along the surface of the isothermal sphere from the lowest point and the y-coordinate is measured normal to the surface, with a denoting the radius of the isothermal sphere. $r(x) = a\sin(x/a)$ is the *radial distance* from the symmetrical axis to the surface of the sphere. The gravitational acceleration $\boldsymbol{g}$, acts downward. We also assume that the Boussineq approximation holds i.e. that density variation is only experienced in the buoyancy term in the momentum equation.

Both isothermal sphere and the Jeffreys fluid are maintained initially at the same temperature and concentration. Instantaneously they are raised to a temperature $T_w > T_\infty$ and concentration $C_w > C_\infty$, where the latter (ambient) temperature and concentration of the fluid are sustained constant. Introducing the boundary layer approximations, the equations for *mass, momentum, energy and species diffusion*, can be written as follows:

$$\frac{\partial(ru)}{\partial x} + \frac{\partial(rv)}{\partial y} = 0 \tag{4}$$

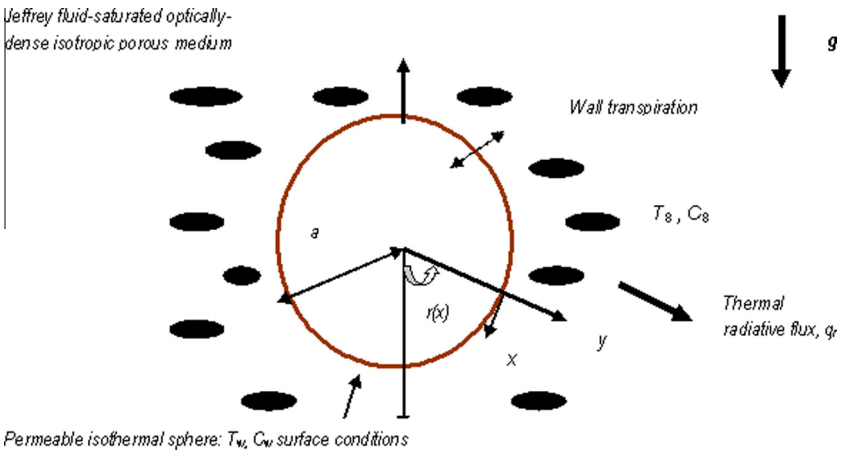

Figure 1 Physical regime and coordinate system.

$$u\frac{\partial u}{\partial x}+v\frac{\partial u}{\partial y}=\frac{\nu}{1+\lambda}\left(\frac{\partial^2 u}{\partial y^2}+\lambda_1\left(u\frac{\partial^3 u}{\partial x\partial y^2}-\frac{\partial u}{\partial x}\frac{\partial^2 u}{\partial y^2}+\frac{\partial u}{\partial y}\frac{\partial^2 u}{\partial x\partial y}+v\frac{\partial^3 u}{\partial y^3}\right)\right) g\beta(T-T_\infty)\sin(x/a)+g\beta^*(C-C_\infty)\sin(x/a) -\frac{\nu}{K}u-\Gamma u^2 \quad (5)$$

$$u\frac{\partial T}{\partial x}+v\frac{\partial T}{\partial y}=\alpha\frac{\partial^2 T}{\partial y^2}-\frac{1}{\rho c_p}\frac{\partial q_r}{\partial y}+\frac{Q_0}{\rho c_p}(T-T_\infty) \quad (6)$$

$$u\frac{\partial C}{\partial x}+v\frac{\partial C}{\partial y}=D_m\frac{\partial^2 C}{\partial y^2} \quad (7)$$

where u and v are the velocity components in the x- and y-directions respectively, $\nu=\mu/\rho$ – the kinematic viscosity of the Jeffreys fluid and the other parameters is mentioned in the nomenclature. The Jeffreys viscoelastic fluid model introduces several *mixed* derivatives into the momentum boundary layer Eq. (5) and in particular two *third order* derivatives, $u\frac{\partial^3 u}{\partial x\partial y^2}$ and $v\frac{\partial^3 u}{\partial y^3}$. The momentum equation therefore attains an order higher than the *classical Navier–Stokes (Newtonian) viscous flow* model. The non-Newtonian effects feature in the shear terms only of Eq. (5). Negating relaxation and retardation effects i.e. $\lambda\to 0$ and $\lambda_1\to 0$ reduces the equation to the conventional Newtonian model. The second term on the right hand side of Eq. (5) represents the *thermal buoyancy force* and couples the velocity field with the temperature field Eq. (6). The third term on right hand side of Eq. (5) represents the *species buoyancy effect (mass transfer)* and couples Eq. (5) to the species diffusion Eq. (7). The fourth and fifth terms on the right hand side of Eq. (5) denote the *Darcian linear drag* and *Forchheimer second-order drag*, respectively. The boundary conditions are prescribed at the sphere surface and the edge of the boundary layer regime, respectively as follows:

$$\begin{aligned} &At \quad y=0, \quad u=0, \quad v=-V_w, \quad T=T_w, \quad C=C_w \\ &As \quad y\to\infty, \quad u\to 0, \quad v\to 0, \quad T\to T_\infty, \quad C\to C_\infty \end{aligned} \quad (8)$$

where T_∞ – the free stream temperature, C_∞ – the free stream concentration, V_w – the uniform blowing/suction velocity representing lateral mass flux (transpiration) at the sphere surface. In Eq. (6) the penultimate term on the right hand side is the *thermal radiation flux contribution* based on the Rosseland approximation [39,40]. This formulation allows the transformation of the governing integro-differential equation for radiative energy balance into a *Fourier-type* diffusion equation analogous to that describing heat conduction or electrostatic potential (Coulomb's law) which is valid for *optically-thick media* in which radiation only propagates a limited distance prior to experiencing scattering or absorption. It can be shown that the local intensity is caused by radiation emanating from nearby locations in the vicinity of which the emission and scattering are comparable to the location under consideration. For zones where conditions are appreciably different, the radiation has been shown to be greatly attenuated prior to arriving at the location being analyzed. The energy transfer depends only on the conditions in the area near the position under consideration. In applying the Rosseland assumption, it is assumed that refractive index of the medium is constant, intensity within the porous medium is nearly isotropic and uniform and wavelength regions exist where the optical thickness is greater than 5. Further details are available in Anwar Bég et al. [40]. The final term on the right hand side of Eq. (6) is the *heat source/sink contribution*. The Rosseland diffusion flux model is an *algebraic approximation* and defined as follows:

$$q_r=\frac{4\sigma^*}{3k^*}\frac{\partial T^4}{\partial y} \quad (9)$$

where k^* – mean absorption coefficient and σ^* – Stefan–Boltzmann constant. It is customary [39] to express T^4 as a linear function of temperature. Expanding T^4 using Taylor series and neglecting higher order terms leads to the following:

$$T^4 \cong 4T_\infty^3 T-3T_\infty^4 \quad (10)$$

Substituting (10) into (9), eventually leads to the following version of the heat conservation Eq. (6):

$$u\frac{\partial T}{\partial x}+v\frac{\partial T}{\partial y}=\alpha\frac{\partial^2 T}{\partial y^2}+\frac{16\sigma^* T_\infty^3}{3k^*\rho c_p}\frac{\partial^2 T}{\partial y^2}+\frac{Q_0}{\rho c_p}(T-T_\infty) \quad (11)$$

The stream function ψ is defined by $ru=\frac{\partial(r\psi)}{\partial y}$ and $rv=-\frac{\partial(r\psi)}{\partial x}$, and therefore, the continuity equation is automatically satisfied. In order to render the governing equations and the boundary conditions in dimensionless form, the following non-dimensional quantities are introduced.

$$\xi = \frac{x}{a}, \quad \eta = \frac{y}{a}\sqrt[4]{Gr}, \quad f(\xi,\eta) = \frac{\psi}{\nu\xi\sqrt[4]{Gr}},$$
$$\theta(\xi,\eta) = \frac{T - T_\infty}{T_w - T_\infty}, \quad \phi(\xi,\eta) = \frac{C - C_\infty}{C_w - C_\infty} \tag{12}$$

In view of the transformation defined in Eq. (12), the boundary layer Eqs. (4)–(7) are reduced to the following seventh order system of coupled, nonlinear, dimensionless partial differential equations for momentum, energy and concentration for the regime:

$$\frac{1}{1+\lambda}f''' + ff''(1+\xi\cot\xi) + \frac{De}{1+\lambda}\left(f''^2 - ff^{iv}(1+\xi\cot\xi)\right) - (1+\Lambda\xi)(f')^2 + \frac{\sin\xi}{\xi}(\theta + N\phi) - \frac{1}{Da}f' = \xi\left(f'\frac{\partial f'}{\partial\xi} - f''\frac{\partial f}{\partial\xi} - \frac{De}{1+\lambda}\left(f'\frac{\partial f'''}{\partial\xi} - f'''\frac{\partial f'}{\partial\xi} + f''\frac{\partial f''}{\partial\xi} - f^{iv}\frac{\partial f}{\partial\xi}\right)\right) \tag{13}$$

$$\frac{\theta''}{P}r\left(1+\frac{4}{3F}\right) + f\theta'(1+\xi\cot\xi) + \Delta\theta = \xi\left(f'\frac{\partial\theta}{\partial\xi} - \theta'\frac{\partial f}{\partial\xi}\right) \tag{14}$$

$$\frac{\phi''}{Sc} + f\phi'(1+\xi\cot\xi) = \xi\left(f'\frac{\partial\phi}{\partial\xi} - \phi'\frac{\partial f}{\partial\xi}\right) \tag{15}$$

The transformed dimensionless boundary conditions are as follows:

$$\begin{aligned} &At \quad \eta = 0, \quad f = f_w, \quad f' = 0, \quad \theta = 1, \quad \phi = 1 \\ &As \quad \eta \to \infty, \quad f' \to 0, \quad f'' \to 0, \quad \theta \to 0, \quad \phi \to 0 \end{aligned} \tag{16}$$

In the above equations, the primes denote the differentiation with respect to η, the dimensionless radial coordinate, ξ is the dimensionless tangential coordinate, $De = \dfrac{\lambda_1 \nu\sqrt{Gr}}{a^2}$ – the Deborah number characterizing the fluidity of the material (viscoelasticity), $\Lambda = \Gamma a$ – the Local inertia coefficient (Forchheimer parameter), $N = \dfrac{\beta^*(C_w - C_\infty)}{\beta(T_w - T_\infty)}$ – the concentration to thermal buoyancy ratio parameter, $Gr = \dfrac{g\beta(T_w - T_\infty)a^3}{\nu^2}$ – the Grashof number, $Da = \frac{K\sqrt{Gr}}{a^2}$ – the Darcy parameter, $Pr = \frac{\rho\nu c_p}{k}$ – the Prandtl number, $F = \dfrac{Kk^*}{4\sigma^* T_\infty^3}$ – the radiation parameter, $\Delta = \dfrac{Q_0 a^2}{\rho\nu c_p\sqrt{Gr}}$ – the dimensionless heat generation/absorption coefficient, $\beta^*(C_w - C_\infty)$ – the Schmidt number, $f_w = -\dfrac{V_w a}{\nu\sqrt[4]{Gr}}$ – the blowing/suction parameter. The engineering design quantities of physical interest include the *skin-friction coefficient* (normalized surface shear stress function), *Nusselt number* (dimensionless surface heat transfer rate) and *Sherwood number* (dimensionless surface mass transfer rate) which are given by the following:

$$\frac{1}{2}C_f Gr^{-3/4} = \xi f''(\xi,0) \tag{17}$$

$$\frac{Nu}{\sqrt[4]{Gr}} = -\theta'(\xi,0) \tag{18}$$

$$\frac{Sh}{\sqrt[4]{Gr}} = -\phi'(\xi,0) \tag{19}$$

The location, $\xi \sim 0$, corresponds to the vicinity of the *lower stagnation point* on the sphere. Since $\frac{\sin\xi}{\xi} \to 0/0$ i.e. 1. For this scenario, the model defined by Eqs. (13)–(15) contracts to an *ordinary* differential boundary value problem:

$$\frac{1}{1+\lambda}f''' + ff'' - \frac{De}{1+\lambda}ff^{iv} + \frac{De}{1+\lambda}f''^2 - f'^2 + (\theta + N\varphi) - \frac{1}{Da}f' = 0 \tag{20}$$

$$\frac{1}{Pr}\left(1+\frac{4}{3F}\right)\theta'' + f\theta' + \Delta\theta = 0 \tag{21}$$

$$\frac{\phi''}{Sc} + f\phi' = 0 \tag{22}$$

The boundary conditions (16) remain unchanged. Inspection of Eq. (20) reveals that Forchheimer effects vanish at the lower stagnation point whereas the Darcian drag force remains. Furthermore *non-Newtonian* effects are retained in the momentum Eq. (20) via the terms featuring λ and De. Even this simplified version of the flow model is strongly non-linear. The general model is solved using a powerful and unconditionally stable finite difference technique introduced by Keller [41]. The Keller-box method has a second order accuracy with arbitrary spacing and attractive extrapolation features.

4. Numerical solution with keller box implicit method

The Keller-box implicit difference method is utilized to solve the nonlinear boundary value problem defined by Eqs. (13)–(15) with boundary conditions (16). Although other powerful numerical methods have been developed for fluid mechanics including differential transform quadrature [20] and network simulation [40], for *parabolic* problems (of which boundary layer flows are an excellent example), Keller's box technique [41] remains of the most applied. Recent diverse implementations of the box scheme include simulations of subsonic thrusters flows [42], aircraft wing aerodynamics [43], stationary convective-diffusion flows [44], magnetohydrodynamics [45], wavy surface convection flows [46], nanofluids [47], drainage sheet flows [48] and rotating flows [49]. Further applications include magneto-convection [50], double-diffusive convection [51] and fuel cell modelling [52]. The Keller-box discretization is *fully coupled* at each step which reflects the physics of parabolic systems – which are also fully coupled. Discrete calculus associated with the Keller-box scheme has also been shown to be fundamentally different from all other mimetic (physics capturing) numerical methods, as elaborated by Keller [41]. The Keller box scheme comprises four stages:

(1) Decomposition of the Nth order partial differential equation system to N first order equations.
(2) Finite Difference Discretization.
(3) Quasilinearization of Non-Linear Keller Algebraic Equations.
(4) Block-tridiagonal Elimination solution of the Linearized Keller Algebraic Equations.

Stage 1: Decomposition of Nth order partial differential equation system to N first order equations

Eqs. (13)–(15) subject to the boundary conditions (16) are first cast as a multiple system of first order differential equations. New dependent variables are introduced:

$$u(x,y)=f',\quad v(x,y)=f'',\quad q(x,y)=f''',\quad s(x,y)=\theta,\\ \theta'=t \text{ and } g(x,y)=\phi \text{ with } g'=p \tag{23}$$

These denote the variables for velocity, temperature and concentration respectively. Now Eqs. (13)–(15) are solved as a set of eight simultaneous differential equations:

$$f'=u \tag{24}$$

$$u'=v \tag{25}$$

$$v'=q \tag{26}$$

$$g'=p \tag{27}$$

$$s'=t \tag{28}$$

$$\frac{1}{1+\lambda}v'+fv(1+\xi\cot\xi)+\frac{De}{1+\lambda}\left(v^2-fq'(1+\xi\cot\xi)\right)\\ -(1+\Lambda\xi)u^2+\frac{\sin\xi}{\xi}(s+Ng)-\frac{1}{Da}u\\ =\xi\left(u\frac{\partial u}{\partial\xi}-v\frac{\partial f}{\partial\xi}-\frac{De}{1+\lambda}\left(u\frac{\partial q}{\partial\xi}-q\frac{\partial u}{\partial\xi}+v\frac{\partial v}{\partial\xi}-q'\frac{\partial f}{\partial\xi}\right)\right) \tag{29}$$

$$\frac{t'}{Pr}\left(1+\frac{4}{3F}\right)+ft(1+\xi\cot\xi)+\Lambda s=\xi\left(u\frac{\partial s}{\partial\xi}-t\frac{\partial f}{\partial\xi}\right) \tag{30}$$

$$\frac{p'}{Sc}+fp(1+\xi\cot\xi)=\xi\left(u\frac{\partial g}{\partial\xi}-p\frac{\partial f}{\partial\xi}\right) \tag{31}$$

where primes denote differentiation with respect to the variable, η. In terms of the dependent variables, the boundary conditions assume the form:

$$\begin{array}{llllll} At & \eta=0, & u=0, & v=f_w, & s=1, & g=1\\ As & \eta\to 0, & u\to 0, & v\to 0, & s\to 0, & g\to 0\end{array} \tag{32}$$

Stage 2: Finite Difference Discretization

A two dimensional computational grid is imposed on the $\xi-\eta$ plane as depicted in Fig. 2. The stepping process is defined by the following:

$$\eta_0=0,\quad \eta_i=\eta_{i-1}+h_j,\quad j=1,2,\ldots,J,\quad \eta_J\equiv\eta_\infty \tag{33}$$

$$\xi^0=0,\quad \xi^n=\xi^{n-1}+k_n,\quad n=1,2,\ldots,N \tag{34}$$

where k_n is the $\Delta\xi$ – spacing and h_j is the $\Delta\eta$ – spacing. If g_j^n denotes the value of any variable at (η_j,ξ^n), then the variables and derivatives of Eqs. (24)–(31) at $\left(\eta_{j-1/2},\xi^{n-1/2}\right)$ are replaced by the following:

$$g_{j-1/2}^{n-1/2}=\frac{1}{4}\left(g_j^n+g_{j-1}^n+g_j^{n-1}+g_{j-1}^{n-1}\right) \tag{35}$$

$$\left(\frac{\partial g}{\partial\eta}\right)_{j-1/2}^{n-1/2}=\frac{1}{2h_j}\left(g_j^n-g_{j-1}^n+g_j^{n-1}-g_{j-1}^{n-1}\right) \tag{36}$$

$$\left(\frac{\partial g}{\partial\xi}\right)_{j-1/2}^{n-1/2}=\frac{1}{2k^n}\left(g_j^n-g_{j-1}^n+g_j^{n-1}-g_{j-1}^{n-1}\right) \tag{37}$$

The resulting finite – difference approximation of Eqs. (24)–(31) for the mid-point $\left(\eta_{j-1/2},\xi^n\right)$, are as follows:

$$h_j^{-1}\left(f_j^n-f_{j-1}^n\right)=u_{j-1/2}^n \tag{38}$$

$$h_j^{-1}\left(u_j^n-u_{j-1}^n\right)=v_{j-1/2}^n \tag{39}$$

$$h_j^{-1}\left(v_j^n-v_{j-1}^n\right)=q_{j-1/2}^n \tag{40}$$

$$h_j^{-1}\left(g_j^n-g_{j-1}^n\right)=p_{j-1/2}^n \tag{41}$$

$$h_j^{-1}\left(s_j^n-s_{j-1}^n\right)=t_{j-1/2}^n \tag{42}$$

$$\frac{(v_j-v_{j-1})}{1+\lambda}+\frac{h_j(1+\alpha+\xi\cot\xi)(f_j+f_{j-1})(v_j+v_{j-1})}{4}\\ +\frac{De}{1+\lambda}\frac{(1+\alpha)h_j}{4}(v_j+v_{j-1})^2\\ -\frac{De(1+\alpha+\xi\cot\xi)(f_j+f_{j-1})(q_j-q_{j-1})}{2(1+\lambda)}\\ -\frac{1}{Da}\frac{h_j}{2}(u_j+u_{j-1})+B\frac{h_j}{2}(s_j+s_{j-1}+N(g_j+g_{j-1}))\\ -\frac{h_j(1+\alpha+\Lambda\xi)}{4}(u_j+u_{j-1})^2-\frac{\alpha h_j}{2}f_{j-1/2}^{n-1}(v_j+v_{j-1})\\ +\frac{\alpha h_j}{2}v_{j-1/2}^{n-1}(f_j+f_{j-1})+\frac{\alpha h_jDe}{1+\lambda}u_{j-1/2}^{n-1}(q_j+q_{j-1})\\ -\frac{\alpha h_jDe}{1+\lambda}q_{j-1/2}^{n-1}(u_j+u_{j-1})+\frac{\alpha De}{1+\lambda}f_{j-1/2}^{n-1}(q_j-q_{j-1})\\ -\frac{\alpha De}{1+\lambda}(q')_{j-1/2}^{n-1}(f_j+f_{j-1})=[R_1]_{j-/12}^{n-1} \tag{43}$$

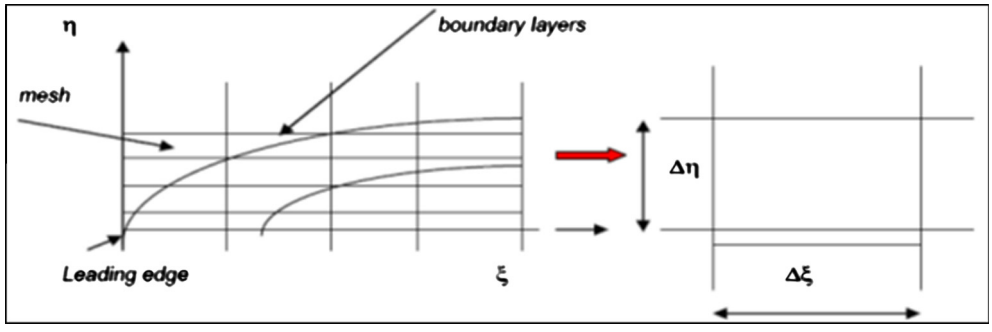

Figure 2 Grid meshing and Keller-box computational cell.

$$\frac{1}{Pr}(t_j - t_{j-1}) + \frac{(1+\alpha+\xi\cot\xi)h_j}{4}(f_j + f_{j-1})(t_j + t_{j-1}) + \frac{\Delta h_j}{2}(s_j - s_{j-1}) - \frac{\alpha h_j}{4}(u_j + u_{j-1})(s_j + s_{j-1}) + \frac{\alpha h_j}{2}s^{n-1}_{j-1/2}(u_j + u_{j-1}) - \frac{\alpha h_j}{2}u^{n-1}_{j-1/2}(s_j + s_{j-1}) - \frac{\alpha h_j}{2}f^{n-1}_{j-1/2}(t_j + t_{j-1}) + \frac{\alpha h_j}{2}t^{n-1}_{j-1/2}(f_j + f_{j-1}) = [R_2]^{n-1}_{j-1/2} \quad (44)$$

$$\frac{1}{Sc}(p_j - p_{j-1}) + \frac{(1+\alpha+\xi\cot\xi)h_j}{4}(f_j + f_{j-1})(p_j + p_{j-1}) - \frac{\alpha h_j}{4}(u_j + u_{j-1})(g_j + g_{j-1}) + \frac{\alpha h_j}{2}g^{n-1}_{j-1/2}(u_j + u_{j-1}) - \frac{\alpha h_j}{2}u^{n-1}_{j-1/2}(g_j + g_{j-1}) - \frac{\alpha h_j}{2}f^{n-1}_{j-1/2}(p_j + p_{j-1}) + \frac{\alpha h_j}{2}p^{n-1}_{j-1/2}(f_j + f_{j-1}) = [R_3]^{n-1}_{j-1/2} \quad (45)$$

where we have used the abbreviations

$$\alpha = \frac{\xi^{n-1/2}}{k_n}, \qquad B = \frac{\sin\left(\xi^{n-1/2}\right)}{\xi^{n-1/2}} \quad (46)$$

$$[R_1]^{n-1}_{j-1/2} = -h_j \begin{bmatrix} \frac{1}{1+\lambda}(v')^{n-1}_{j-1/2} + (1-\alpha+\xi\cot\xi)f^{n-1}_{j-1/2}v^{n-1}_{j-1/2} + \frac{De}{1+\lambda}(1-\alpha)\left(v^{n-1}_{j-1}\right)^2 \\ -\frac{1}{Da}u^{n-1}_{j-1/2} - \frac{De}{1+\lambda}(1-\alpha+\xi\cot\xi)f^{n-1}_{j-1/2}(q')^{n-1}_{j-1/2} + B\left(s^{n-1}_{j-1/2} + Ng^{n-1}_{j-1/2}\right) \\ -(1-\alpha+\Lambda\xi)\left(u^{n-1}_{j-1/2}\right)^2 \end{bmatrix} \quad (47)$$

$$[R_2]^{n-1}_{j-1/2} = -h_j\left[\frac{1}{Pr}\left(1+\frac{4}{3F}\right)(t')^{n-1}_{j-1/2} + (1-\alpha+\xi\cot\xi)f^{n-1}_{j-1/2}t^{n-1}_{j-1/2} + \Delta s^{n-1}_{j-1/2} + \alpha u^{n-1}_{j-1/2}s^{n-1}_{j-1/2}\right] \quad (48)$$

$$[R_3]^{n-1}_{j-1/2} = -h_j\left[\frac{1}{Sc}(p')^{n-1}_{j-1/2} + (1-\alpha+\xi\cot\xi)f^{n-1}_{j-1/2}p^{n-1}_{j-1/2} + \alpha u^{n-1}_{j-1/2}g^{n-1}_{j-1/2}\right] \quad (49)$$

The boundary conditions are as follows:

$$f^n_0 = u^n_0 = 0, \quad s^n_0 = 1, \quad g^n_0 = 1, \quad u^n_J = 0, \quad v^n_J = 0, \quad s^n_J = 0, \quad g^n_0 = 0 \quad (50)$$

Stage 3: Quasilinearization of Non-Linear Keller Algebraic Equations

If we assume f^{n-1}_j, u^{n-1}_j, v^{n-1}_j, q^{n-1}_j, g^{n-1}_j, p^{n-1}_j, s^{n-1}_j, t^{n-1}_j to be known for $0 \leqslant j \leqslant J$, this leads to a system of $8J+8$ equations for the solution of $8J+8$ unknowns f^n_j, u^n_j, v^n_j, q^n_j, g^n_j, p^n_j, s^n_j, t^n_j, $j = 0, 1, 2, \ldots, J$. This non-linear system of algebraic equations is linearized by means of Newton's method, as described by Takhar et al. [31].

Stage 4: Block-tridiagonal Elimination Solution of Linear Keller Algebraic Equations

The linearized system is solved by the block-elimination method, since it possess a block-tridiagonal structure. The bock-tridiagonal structure generated consists of *block matrices*. The complete linearized system is formulated as a *block matrix system*, where each element in the coefficient matrix is a matrix itself, and this system is solved using the efficient Keller-box method. The numerical results are strongly influenced by the number of mesh points in both directions. After some trials in the η – direction (radial coordinate) a larger number of mesh points are selected whereas in the ξ – direction (tangential coordinate) significantly less mesh points are utilized. η_{max} has been set at 10 and this defines an adequately large value at which the prescribed boundary conditions are satisfied. ξ_{max} is set at 3.0 for this flow domain. Mesh independence is achieved in the present computations. The numerical algorithm is executed in **MATLAB** on a PC. The method demonstrates excellent stability, convergence and consistency, as elaborated by Keller [41].

5. Numerical results and interpretation

Comprehensive solutions have been obtained and are presented in Tables 1–3 and Figs. 3(a)–11(c). The numerical problem comprises two independent variables (ξ, η), three dependent fluid dynamic variables (f, θ, ϕ) and eleven thermo-physical and body force control parameters, namely, De, λ, Da, Λ, Pr, F, Δ, Sc, N, f_w. The following default parameter values i.e., $De = 0.1$, $\lambda = 0.2$, $Da = 0.1$, $\Lambda = 0.1$, $Pr = 0.71$, $F = 0.5$, $\Delta = 0.1$, $Sc = 0.6$, $N = 0.5$, $f_w = 0.5$ are prescribed (unless otherwise stated). Furthermore the influence of stream wise (transverse) coordinate on heat and mass transfer characteristics is investigated. A low Deborah number ($De = 0.1$) is prescribed to simulate *weakly elastic* effects in the fluid.

In Table 1, we present the influence of Deborah number, De, on skin friction, heat transfer rate and mass transfer rate, along with a variation in mass flux parameter (f_w), Schmidt number (Sc) and transverse coordinate (ξ). With increasing Deborah number skin friction is markedly reduced owing to the increase in elasticity effects. This also serves to reduce boundary layer thickness as the flow is decelerated. Similarly heat transfer rates are also diminished with increasing Deborah numbers. A significant reduction in wall mass transfer rates (local Sherwood number function) also accompanies a rise in Deborah number. Momentum, thermal and species diffusion are therefore all inhibited with increasing elastic effects. An increase in wall suction ($f_w > 0$) also decreases skin friction whereas it accentuates the heat transfer rate and mass transfer rate at the sphere surface. Increasing Schmidt number which implies a decrease in mass diffusivity of the species is observed to suppress skin friction and heat transfer rates whereas it enhances the mass transfer rates. For $Sc < 1$ species diffusion rate exceeds the momentum diffusion rate and vice versa for $Sc > 1$. For $Sc = 1$ both diffusion rates are the same and the momentum and concentration boundary layer thicknesses equal in the regime. We further note that in Table 1 since Pr is less than unity, thermal diffusivity will exceed momentum diffusivity. With increasing ξ values there is also a decrease in heat transfer rate whereas the skin friction is consistently boosted. The boundary layer flow is therefore accelerated with progressive migration from the lower stagnation point. Mass transfer rate is found to decrease significantly with increasing transverse coordinate.

Table 2 provides results for the influence of the ratio of relaxation to retardation times (λ), Schmidt number (Sc) and Darcy number (Da) on skin friction, heat and mass transfer rates. Skin friction is strongly boosted as are heat transfer and mass transfer rates as the relaxation time is increased (or

Table 1 Values of C_f, Nu and Sh for different De, Sc and $\xi(\lambda = 0.2, Da = 0.1, Pr = 0.71, N = 0.5, F = 0.5, \Lambda = 0.1, \Delta = 0.1)$.

De	f_w	Sc	$\xi = 0^0$			$\xi = 30^0$			$\xi = 60^0$		
			C_f	Nu	Sh	C_f	Nu	Sh	C_f	Nu	Sh
0.1	0.5	0.6	0	0.2421	0.7078	0.2124	0.2308	0.6748	0.3812	0.2001	0.5826
0.5			0	0.2388	0.6987	0.1535	0.2280	0.6669	0.2828	0.1986	0.5779
1.0			0	0.2365	0.6926	0.1248	0.2260	0.6614	0.2334	0.1975	0.5742
1.5			0	0.2348	0.6884	0.1090	0.2246	0.6577	0.2055	0.1966	0.5716
2.0			0	0.2335	0.6853	0.0999	0.2235	0.6548	0.1891	0.1959	0.5695
2.5			0	0.2325	0.6827	0.0907	0.2226	0.6525	0.1726	0.1953	0.5678
3.0			0	0.2316	0.6805	0.0846	0.2218	0.6505	0.1617	0.1948	0.5663
0.1	0.2	0.6	0	0.1424	0.3381	0.2317	0.1362	0.3236	0.4062	0.1200	0.2844
	0.2		0	0.1648	0.4213	0.2279	0.1576	0.4026	0.4007	0.1383	0.3517
	0.3		0	0.1889	0.5115	0.2336	0.1805	0.4882	0.3947	0.1577	0.4245
	0.4		0	0.2147	0.6074	0.2190	0.2049	0.5793	0.3882	0.1784	0.5018
	0.8		0	0.3326	1.0281	0.1981	0.3164	0.9787	0.3851	0.2715	0.8392
	1.0		0	0.3987	1.2515	0.1868	0.3788	1.1906	0.3416	0.3234	1.0178
0.1	0.5	0.25	0	0.2479	0.3489	0.2220	0.2360	0.3344	0.3928	0.2038	0.2948
		0.75	0	0.2407	0.8603	0.2112	0.2295	0.8198	0.3766	0.1991	0.7067
		1.0	0	0.2390	1.1115	0.2068	0.2279	1.0589	0.3698	0.1977	0.9112
		2.0	0	0.2360	2.1027	0.1936	0.2250	2.0011	0.3486	0.1951	1.7133
		3.0	0	0.2349	3.0907	0.1848	0.2239	2.9392	0.3337	0.1941	2.5081
		5.0	0	0.2341	5.0716	0.1739	0.2231	4.8189	0.3144	0.1933	4.0964

Table 2 Values of C_f, Nu and Sh for different λ, Sc and $Da(De = 0.1, \xi = 1.0, Pr = 0.71, N = 0.5, F = 0.5, f_w = 0.5, \Lambda = 0.1, \Delta = 0.1)$.

λ	Sc	$Da = 0.1$			$Da = 1.0$			$Da = 2.0$		
		C_f	Nu	Sh	C_f	Nu	Sh	C_f	Nu	Sh
0.0	0.6	0.3452	0.1996	0.5809	0.8607	0.2896	0.7388	0.9677	0.3058	0.7638
1.0		0.5015	0.2014	0.5866	1.3836	0.3011	0.7706	1.5739	0.3187	0.7998
3.0		0.7230	0.2027	0.5909	2.2060	0.3098	0.7971	2.5345	0.3284	0.8300
5.0		0.8932	0.2033	0.5929	2.8840	0.3138	0.8099	3.3294	0.3328	0.8445
8.0		1.1017	0.2038	0.5946	3.7538	0.3170	0.8208	4.3510	0.3364	0.8569
10.0		1.2217	0.2040	0.5954	4.2692	0.3184	0.8255	4.9569	0.3379	0.8622
15.0		1.4805	0.2043	0.5966	5.4097	0.3206	0.8331	6.2984	0.3404	0.8709
0.2	0.25	0.3928	0.2038	0.2948	1.0392	0.3044	0.4036	1.1736	0.3213	0.4217
	0.75	0.3766	0.1991	0.7067	0.9583	0.2906	0.8811	1.0814	0.3074	0.9090
	1.0	0.3698	0.1977	0.9112	0.9352	0.2882	1.0946	1.0566	0.3051	1.1248
	2.0	0.3486	0.1951	1.7133	0.8806	0.2840	1.9039	0.9995	0.3012	1.9380
	3.0	0.3337	0.1941	2.5081	0.8512	0.2824	2.6915	0.9694	0.2998	2.7263
	5.0	0.3144	0.1933	4.0964	0.8192	0.2812	4.2589	0.9371	0.2986	4.2922

the retardation time decreased). The polymer flows *faster* resulting in accelerated boundary layer flow, and heat and species are diffused more efficiently *to* the sphere surface. Increasing Schmidt number depresses the skin friction and heat transfer rate whereas it increases the mass transfer rate. The decrease in species diffusivity contributes to a reduction in mass transfer at the sphere surface. A similar influence of Schmidt number on momentum and species diffusion fields was also observed by Anwar Bég and Makinde [4]. With increasing Darcy number, skin friction, heat and mass transfer rates are all increased. The, Darcy number, $Da = \frac{K\sqrt{Gr}}{a^2}$ is a bulk porous media parameter and directly proportional to the permeability of the porous medium. It appears in the *linear* Darcian drag force term, $-\frac{1}{Da}f'$ in the momentum Eq. (13). The Darcian drag is inversely proportional to Da. As Da is increased the medium becomes more permeable and there is a decrease in the presence of solid fibers. This decreases the Darcian drag and serves to accelerate the flow in the boundary layer leading to a rise in skin friction. The fluid is able to flow more easily through the porous medium as described by Sochi [7]. This will also aid in enhancing heat transfer and mass transfer from the porous material *to* the sphere surface (it will decrease temperatures and concentrations in the medium, as described later). In table 2 the computations are given for a location some distance from the lower stagnation point i.e. at $\xi = 1$.

Table 3 presents the influence of the ratio of relaxation to retardation times (λ), Prandtl number (Pr) and transverse coordinate (ξ) on skin friction, heat and mass transfer rates. It is again observed that with a rise in the value of λ, skin friction, heat and mass transfer rates are all elevated. Hayat et al. [5] also observed the beneficial contribution of increased

Table 3 Values of C_f, Nu and Sh for different λ, Pr and $\xi(De = 0.1, \xi = 1.0, Pr = 0.71, N = 0.5,\ F = 0.5,\ f_w = 0.5,\ \Lambda = 0.1,\ \Delta = 0.1)$.

λ	Pr	$\xi = 0^0$			$\xi = 30^0$			$\xi = 60^0$		
		C_f	Nu	Sh	C_f	Nu	Sh	C_f	Nu	Sh
0.0	0.6	0	0.2413	0.7055	0.1938	0.2301	0.6726	0.3452	0.1996	0.5809
1.0		0	0.2441	0.7138	0.2823	0.2326	0.6802	0.5015	0.2014	0.5866
3.0		0	0.2462	0.7205	0.4080	0.2345	0.6862	0.7230	0.2027	0.5909
5.0		0	0.2472	0.7237	0.5046	0.2354	0.6891	0.8932	0.2033	0.5929
8.0		0	0.2481	0.7264	0.6229	0.2361	0.6916	1.1017	0.2038	0.5946
10.0		0	0.2484	0.7276	0.6909	0.2364	0.6926	1.2217	0.2040	0.5954
15.0		0	0.2490	0.7296	0.8378	0.2370	0.6944	1.4805	0.2043	0.5966
0.2	0.5	0	0.2013	0.7114	0.2162	0.1935	0.6779	0.3838	0.1724	0.5846
	1.0	0	0.3046	0.7028	0.2111	0.2886	0.6703	0.3771	0.2445	0.5796
	2.0	0	0.5505	0.6870	0.1999	0.5190	0.6558	0.3612	0.4310	0.5688
	3.0	0	0.8134	0.6751	0.1893	0.7679	0.6446	0.3453	0.6391	0.5596
	5.0	0	1.3464	0.6604	0.1715	1.2739	0.6304	0.3175	1.0671	0.5469
	7.0	0	1.8815	0.6521	0.1575	1.7817	0.6223	0.2948	1.4966	0.5392
	10.0	0	2.6874	0.6453	0.1413	2.5462	0.6156	0.2678	2.1418	0.5323

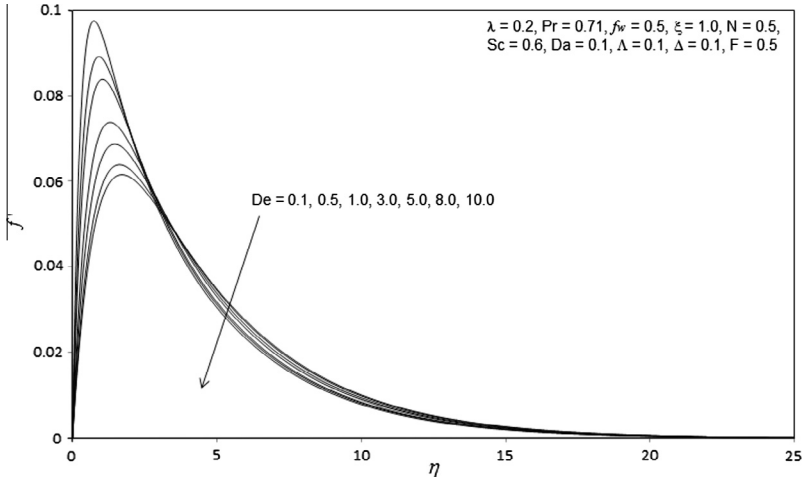

Figure 3(a) Influence of De on velocity profiles.

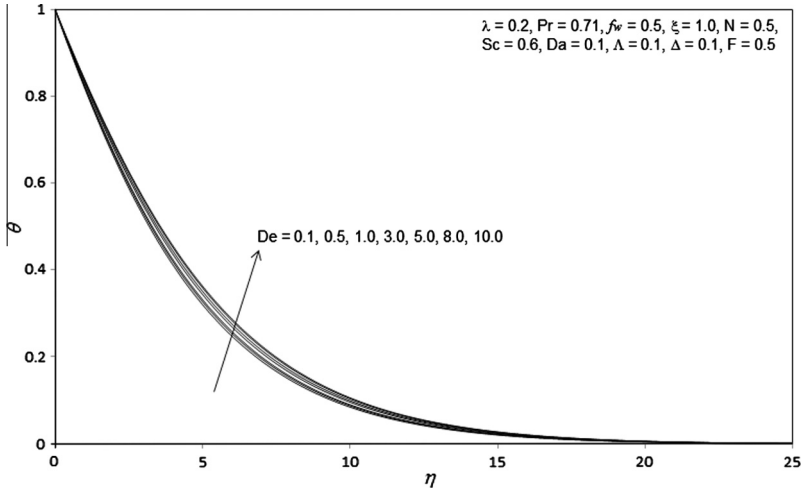

Figure 3(b) Influence of De on temperature profiles.

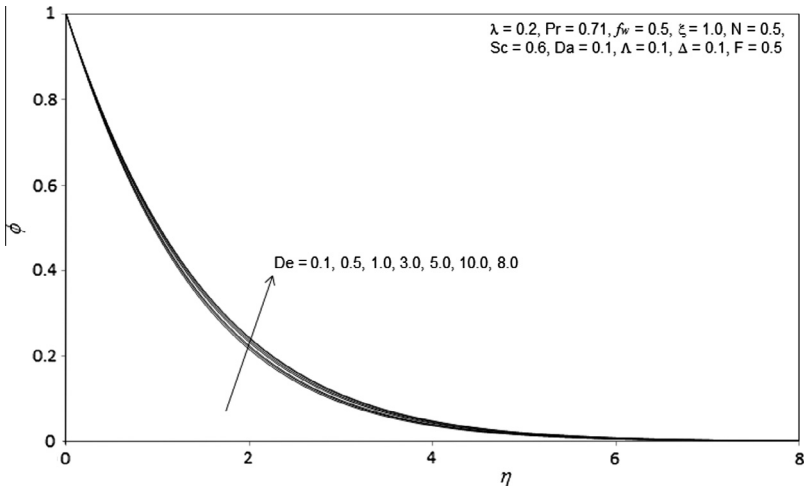

Figure 3(c) Influence of *De* on concentration profiles.

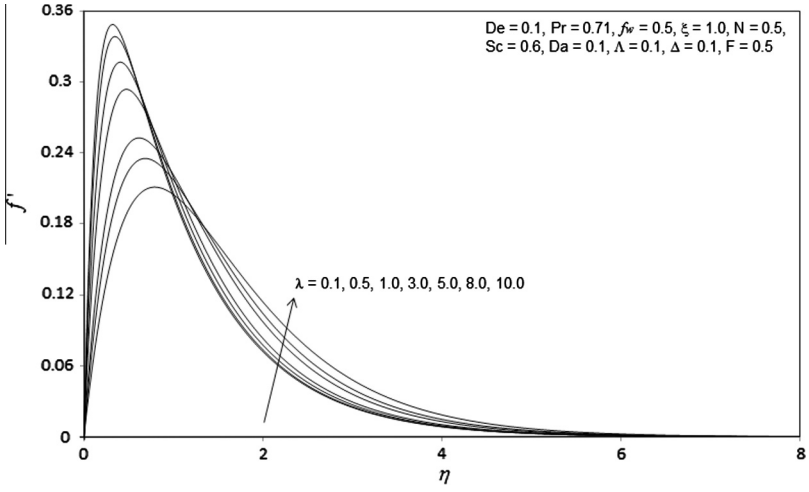

Figure 4(a) Influence of λ on velocity profiles.

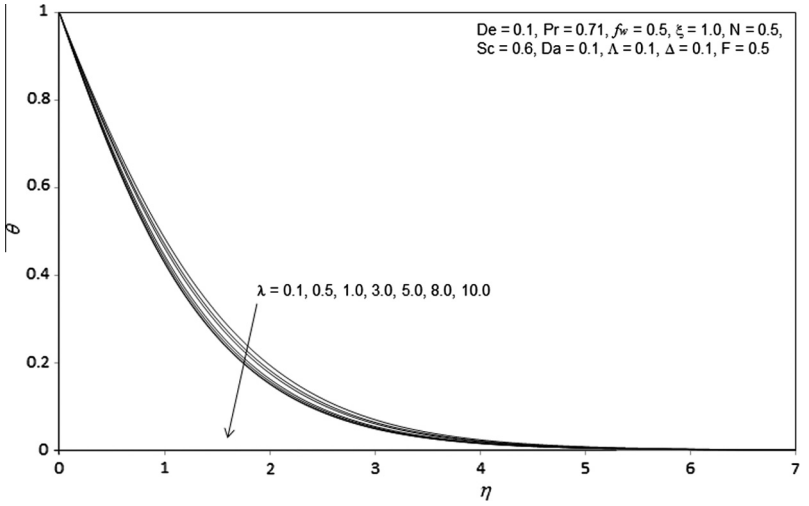

Figure 4(b) Influence of λ on temperature profiles.

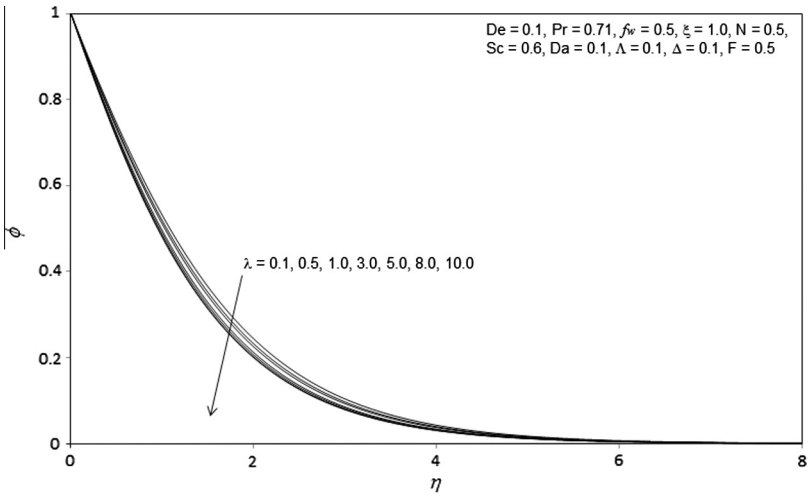

Figure 4(c) Influence of λ on concentration profiles.

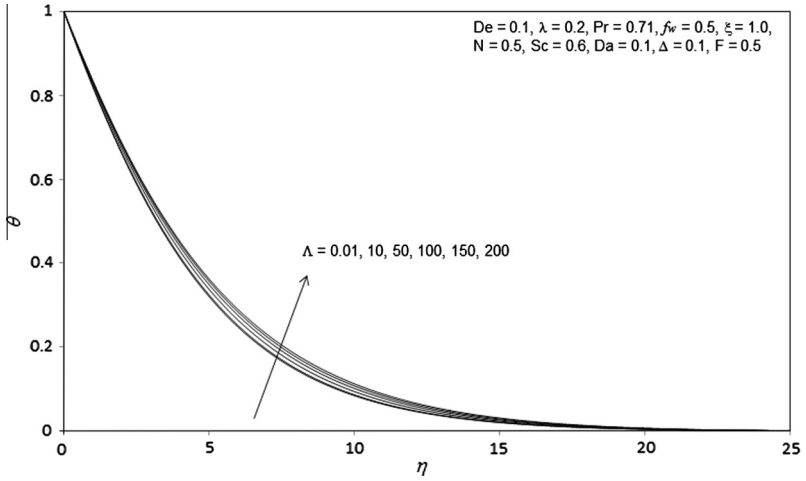

Figure 5(a) Influence of Λ on velocity profiles.

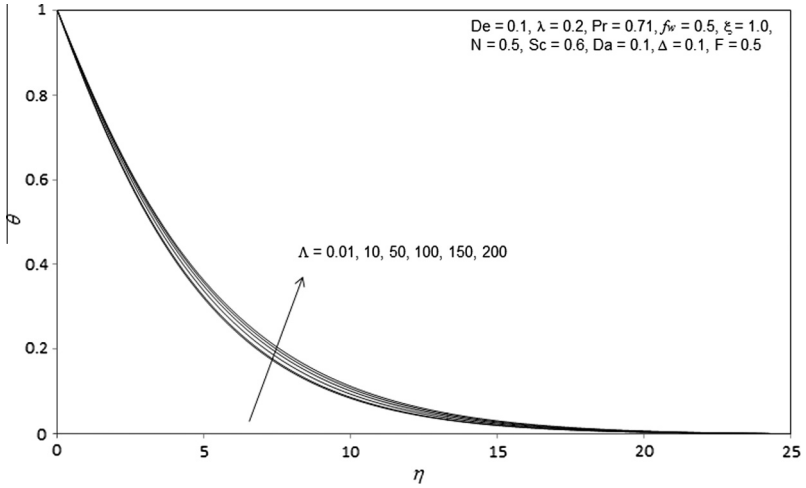

Figure 5(b) Influence of Λ on temperature profiles.

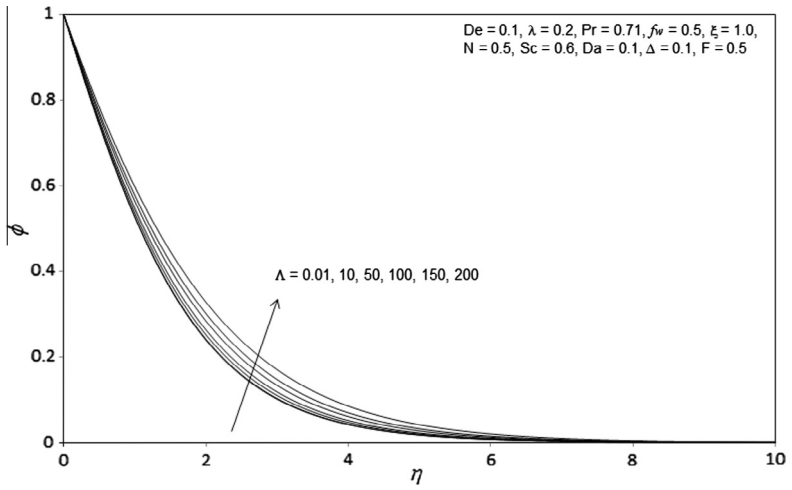

Figure 5(c) Influence of Λ on concentration profiles.

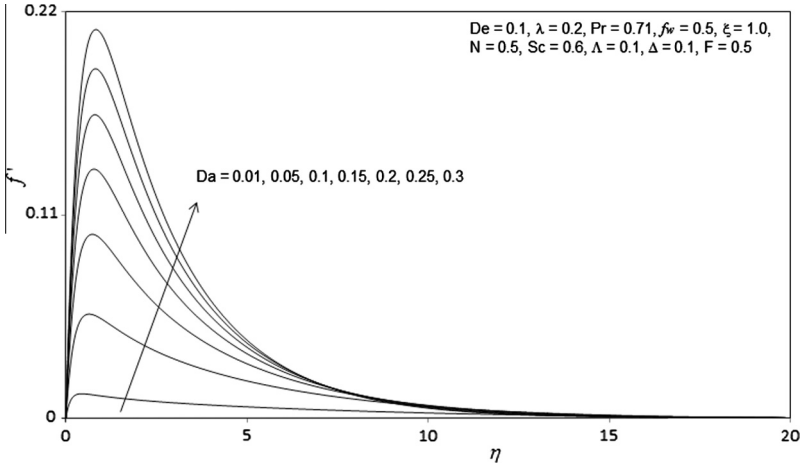

Figure 6(a) Influence of *Da* on velocity profiles.

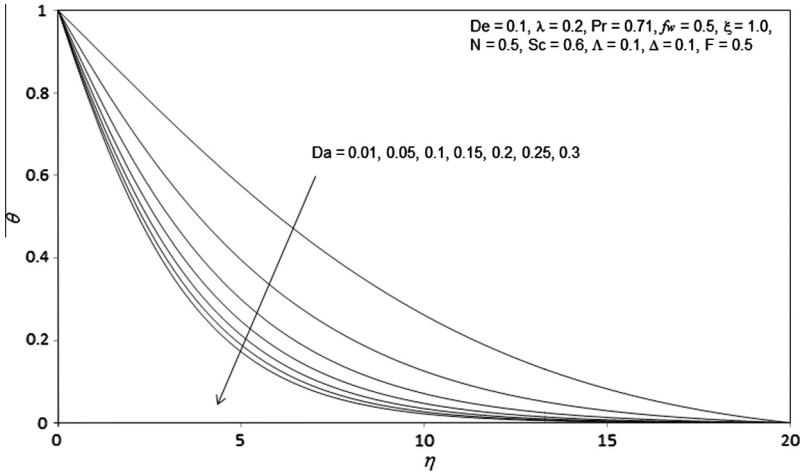

Figure 6(b) Influence of *Da* on temperature profiles.

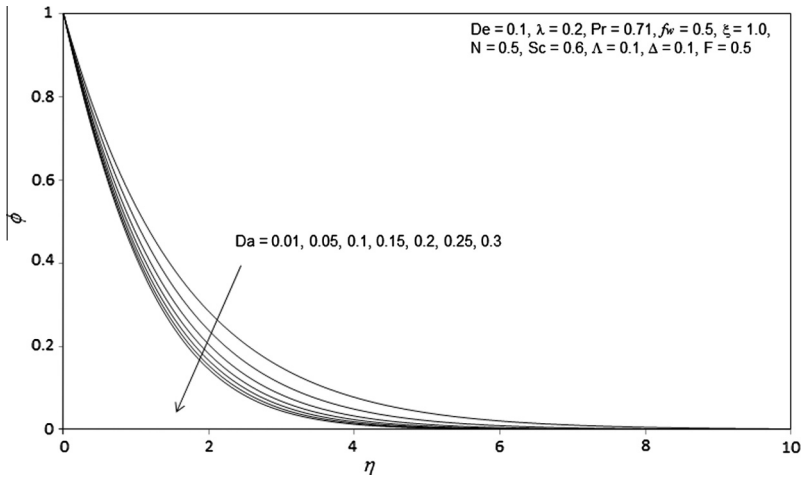

Figure 6(c) Influence of *Da* on concentration profiles.

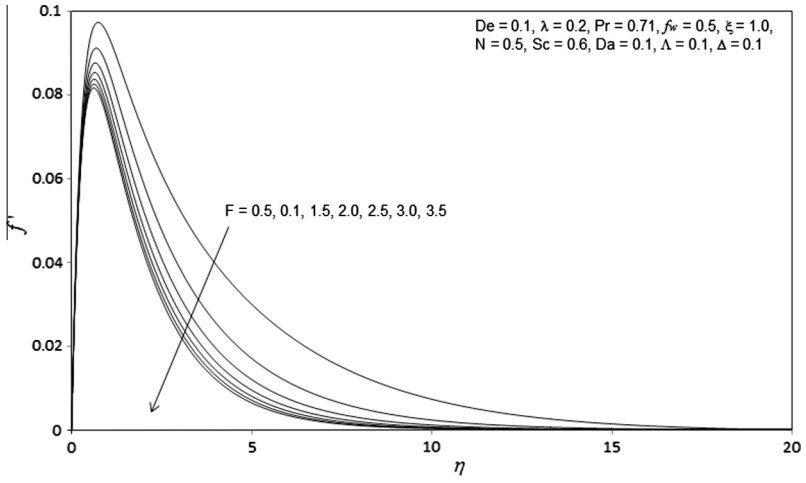

Figure 7(a) Influence of *F* on velocity profiles.

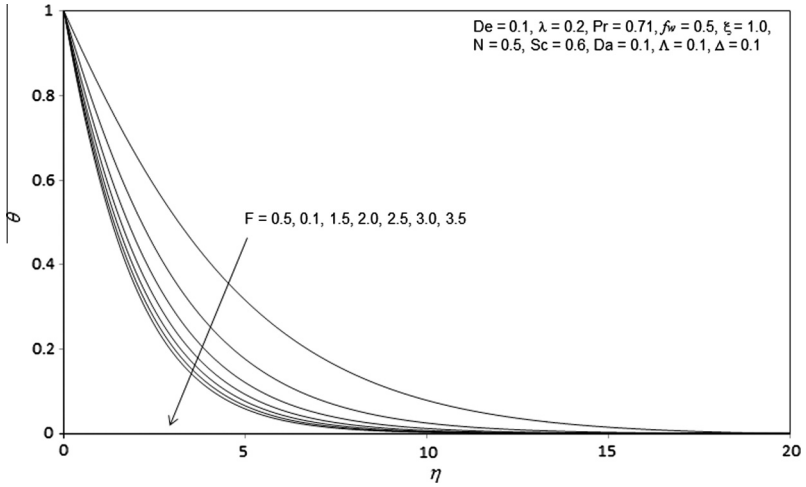

Figure 7(b) Influence of *F* on temperature profiles.

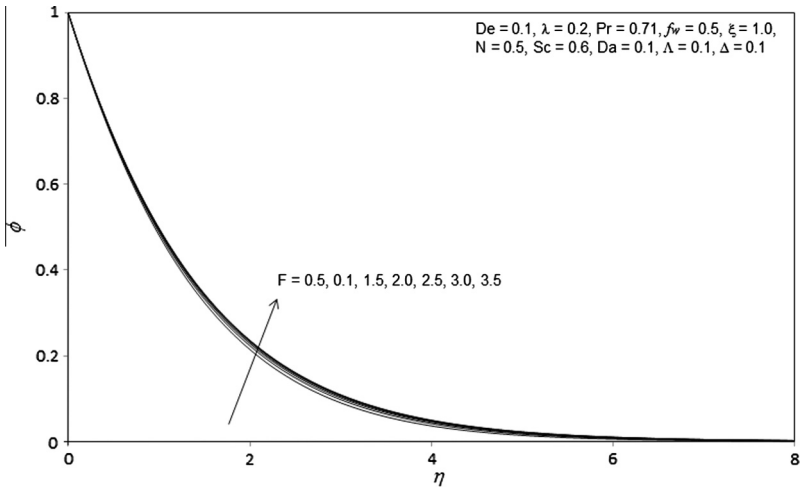

Figure 7(c) Influence of F on concentration profiles.

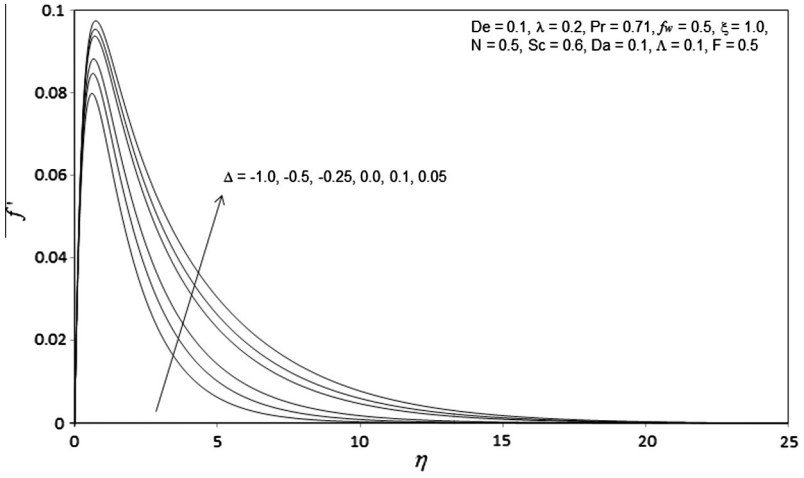

Figure 8(a) Influence of Δ on velocity profiles.

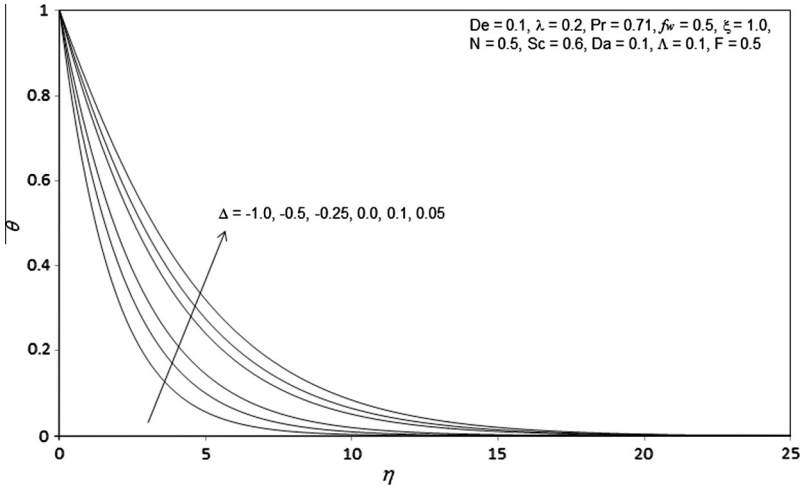

Figure 8(b) Influence of Δ on temperature profiles.

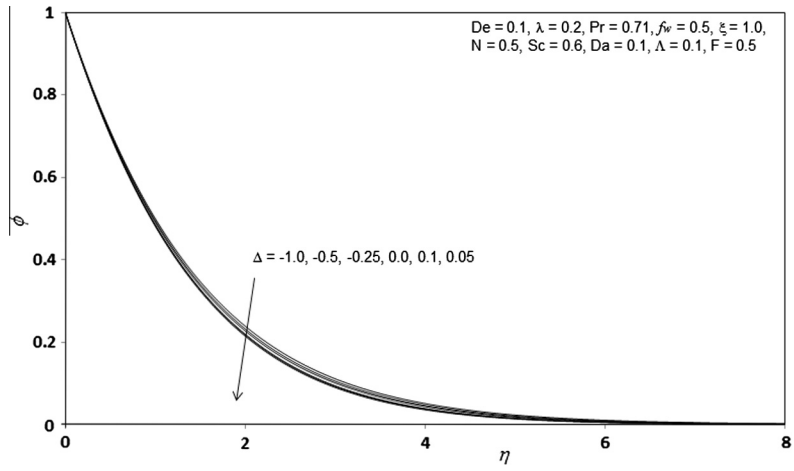

Figure 8(c) Influence of Δ on concentration profiles.

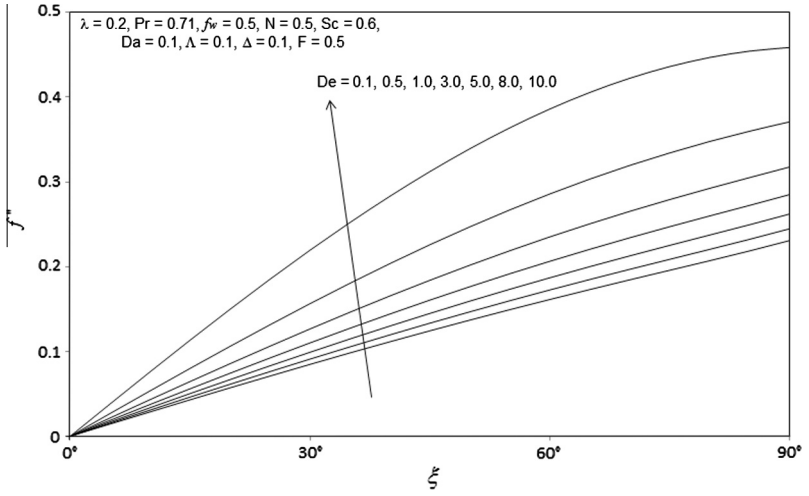

Figure 9(a) Influence of *De* on local skin friction number.

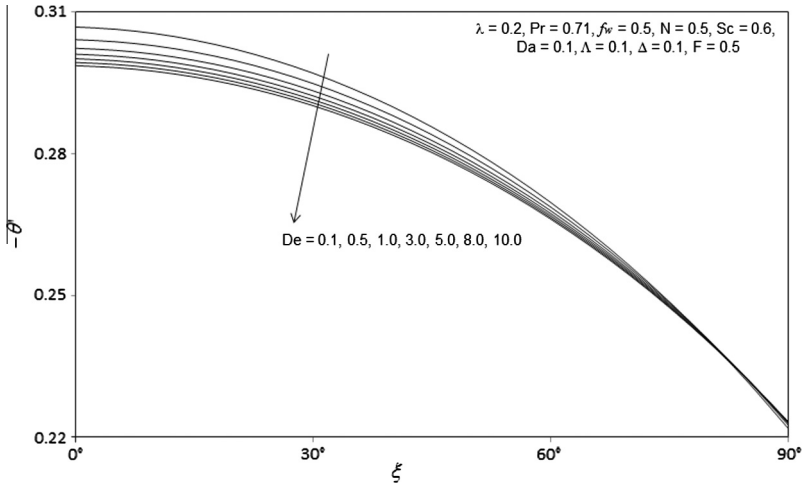

Figure 9(b) Influence of *De* on Nusselt number.

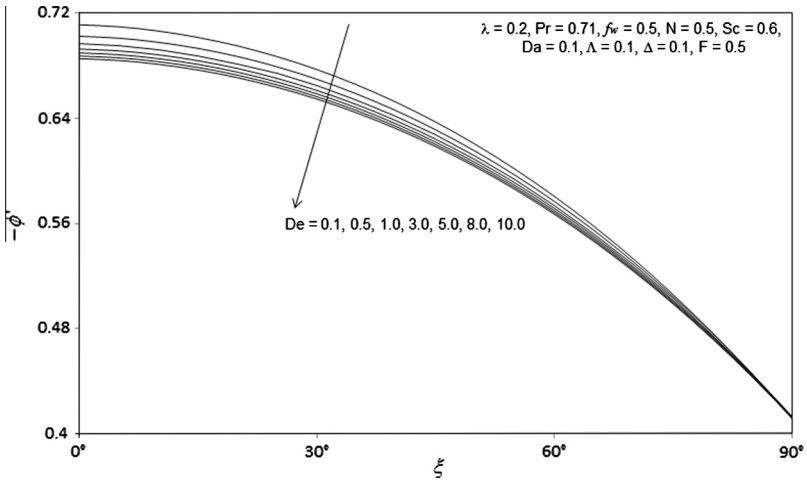

Figure 9(c) Influence of *De* on Sherwood number.

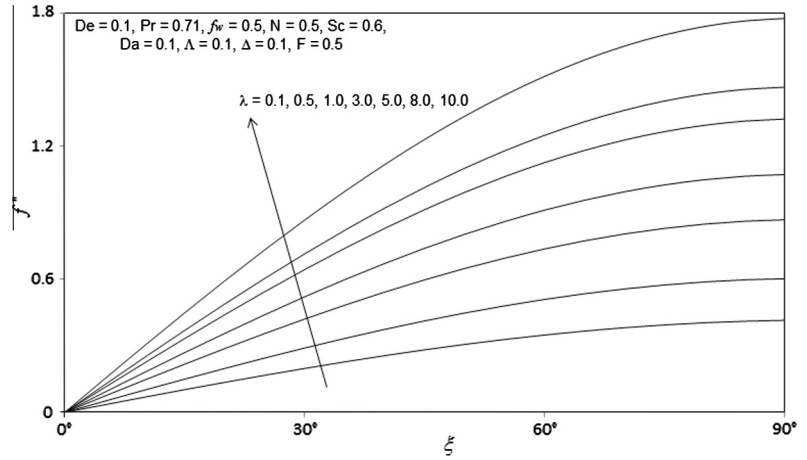

Figure 10(a) Influence of λ on local skin friction number.

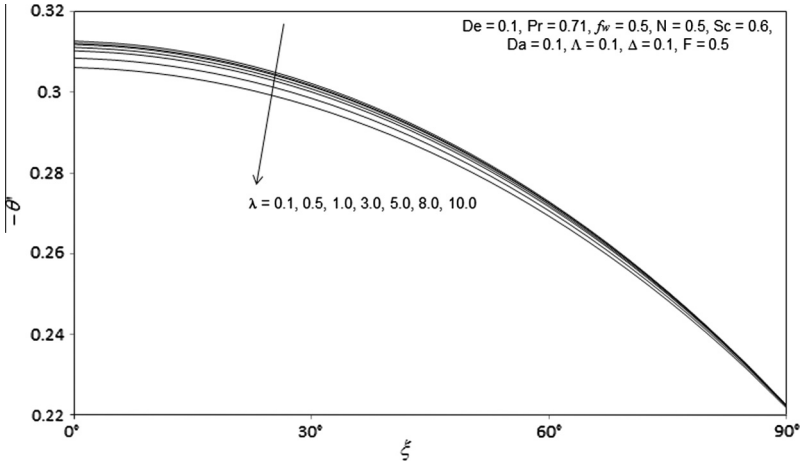

Figure 10(b) Influence of λ on Nusselt number.

relaxation in Jeffrey viscoelastic fluids to heat diffusion, although they did not consider *mass* diffusion. The fact that a rise in λ physically implies a fall in *retardation* time in the fluid and also assists in momentum development. An increase in Prandtl number (*Pr*) strongly accelerates the flow i.e. boosts the skin friction, whereas it decreases the surface heat and

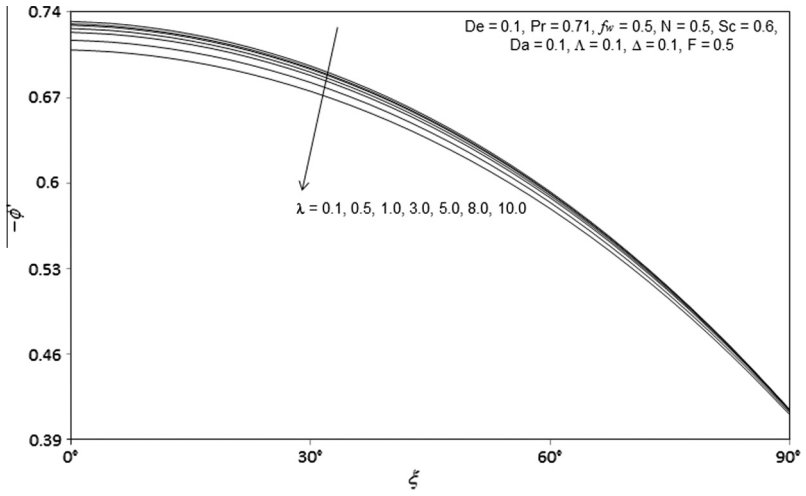

Figure 10(c) Influence of λ on Sherwood number.

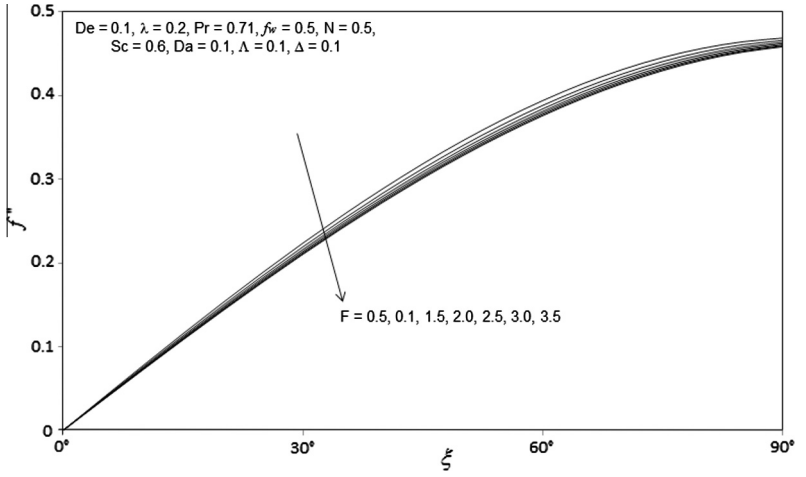

Figure 11(a) Influence of F on local skin friction number.

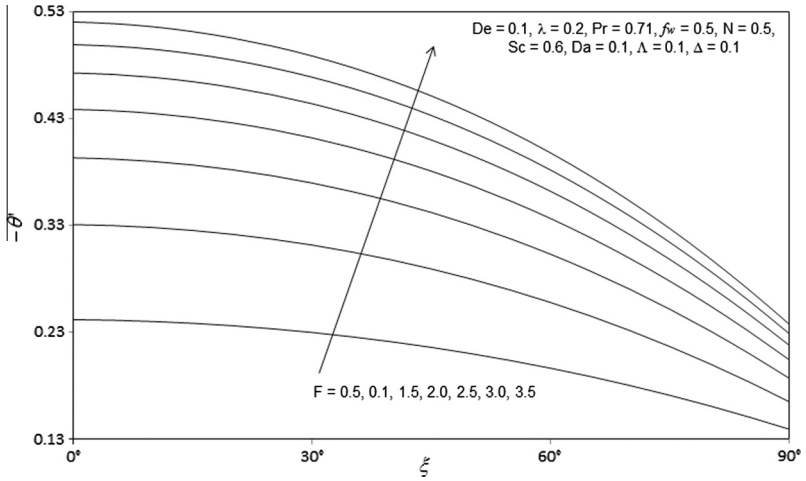

Figure 11(b) Influence of F on Nusselt number.

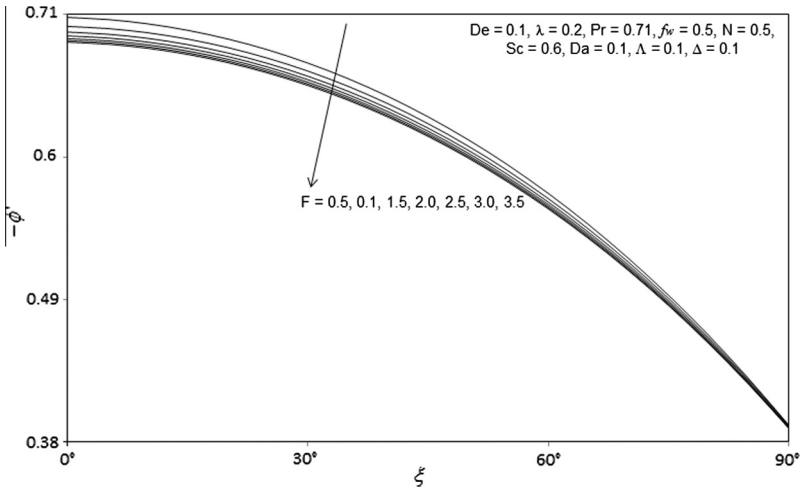

Figure 11(c) Influence of F on Sherwood number.

mass transfer rates. Pr symbolizes the relative rate of momentum diffusion to thermal diffusion in the non-Newtonian fluid. For $Pr < 1$, heat diffuses faster than momentum and vice versa for $Pr > 1$. Higher Pr values also imply a lower thermal conductivity of the non-Newtonian fluid. Increasing Pr therefore leads to heating of the fluid saturated porous regime and a drop in heat transfer rate to the sphere surface (more thermal energy is retained in the porous medium). With increasing values in ξ, there is a strong acceleration in the flow and elevation in skin friction at the sphere surface. Mass transfer rate and heat transfer rate are however reduced with increasing tangential coordinate. Both heat and mass transfer rates attain a maximum at the lower stagnation point ($\xi \sim 0$).

Fig. 3(a)–3(c), illustrates the influence of Deborah number, De, on velocity (f'), temperature (θ) and concentration (ϕ). Dimensionless velocity component (Fig. 3(a)) at the wall is strongly reduced with an increase in De. There will be a corresponding decrease in the momentum (velocity) boundary layer thickness. The influence of De is evidently more pronounced closer to the sphere surface ($\eta = 0$). Smooth decays of the velocity profiles are observed into the free stream demonstrating excellent convergence of the numerical solution. De features in a number of high order derivatives in the momentum boundary layer equation, (13) viz. $\frac{De}{1+\lambda} f f^{iv}(1 + \xi \cot \xi)$, $\frac{De}{1+\lambda} f''^2$ and also $\xi\left(-\frac{De}{1+\lambda}\left[f'\frac{\partial f'''}{\partial \xi} - f'''\frac{\partial f'}{\partial \xi} + f''\frac{\partial f''}{\partial \xi} - f^{iv}\frac{\partial f}{\partial \xi}\right]\right)$. This parameter therefore exerts a strong influence on the *shearing characteristics* of the polymer flow. For non-Newtonian fluids (e.g. polymers), higher De values correspond to the polymer becoming *highly oriented* in one direction and stretched and this is known to occur when the polymer takes longer to relax in comparison with the rate at which the flow is deforming it. Stretching of such fluids causes a lapse in their return to the *unstressed* state. For very high Deborah numbers, the fluid movement is too fast for elastic forces to relax and the material then behaves as a purely elastic solid. As such high Deborah numbers are inappropriate for *viscoelastic flows*. For small Deborah numbers, the time scale of fluid movement is much greater than the relaxation time of elastic forces in the polymer and the polymer then behaves as a *simple viscous fluid*. Fig. 3(b) indicates that an increase in De significantly enhances temperature in the flow field. Temperature profiles consistently decay monotonically from a maximum at the sphere surface to the free stream. All profiles converge at large value of radial coordinate, again showing that convergence has been achieved in the numerical computations. Fig. 3(c) shows a slight increase in concentration is achieved with increasing De values i.e. greater elasticity effects benefit species diffusion.

Fig. 4(a)–4(c) illustrates the effect of the parameter ratio of relaxation to retardation times (λ) on velocity (f'), temperature (θ) and concentration (ϕ) distributions through the boundary layer regime. Velocity is significantly enhanced with increasing λ, in particular close to the sphere surface. Conversely temperature and concentration are markedly reduced with increasing λ. The parameter, λ, also arises in many terms in the momentum Eq. (13) for example $\frac{1}{1+\lambda} f'''$, $-\frac{De}{1+\lambda} f f^{iv}$, $\frac{De}{1+\lambda} f''^2$, etc. It is therefore expected to exert a tangible influence on the flow characteristics. Increasing relaxation times (decreasing retardation times) assists in momentum development in the boundary layer whereas they oppose thermal and mass diffusion. Velocity boundary layer thickness will be *increased* for higher values of λ. Whereas thermal and concentration boundary layer thicknesses will be *reduced*.

Fig. 5(a)–5(c) presents typical profiles for velocity (f'), temperature (θ) and concentration (ϕ) for various values of Forchheimer inertial parameter Λ. This parameter is associated with the second order Forchheimer resistance term, $-\xi\Lambda(f')^2$ in the momentum Eq. (13). Forchheimer drag is directly proportional to the parameter, Λ. An increase in Λ markedly *decelerates* the flow as illustrated in Fig. 5(a), for some considerable distance into the in the boundary layer, transverse to the sphere surface. Inertial quadratic drag has a stronger effect closer to the wall. Kaviany [53] has indicated that Forchheimer effects are associated with higher velocities in porous media transport. Forchheimer drag however is second order and the increase in this "form" drag effectively swamps the momentum development, thereby decelerating the flow, in particular near the sphere surface. The term "non-Darcian" does not allude to a different regime of flow, but to the *amplified* effects of Forchheimer drag at higher velocities, as elaborated also in Anwar Bég et al. [18] and Prasad et al. [45]. With a dramatic increase in Λ there is also

Table 4 Values of heat transfer rate (Nu) for various values of ξ with $N = 0$, $\Lambda = 0$, $Da \to \infty$, $f_w = 0$, $F \to \infty$, $De = 0$, $\lambda = 0$, $Sc = 0.6$, $Pr = 0.71$ between the present results with the solutions reported by Huang and Chen [50].

Pr	ξ	Huang and Chen [50]	Present results
0.7	0^0	1.2276	1.2280
	30^0	1.2031	1.2032
	60^0	1.1296	1.1302
	90^0	1.0071	1.0074
7.0	0^0	0.5165	0.5158
	30^0	0.5065	0.5063
	60^0	0.4768	0.4764
	90^0	0.4276	0.4271

a slight elevation in temperatures (Fig. 5(b)) in the regime. The deceleration in the flow generates a decrease in momentum boundary layer thickness which aids in energy diffusion and a thickening in the thermal boundary layer. The influence on the concentration (species diffusion) field (Fig. 5(c)) is similar to that of the temperature field. However with the same increment in Forchheimer parameter, greater disparity in concentration profiles is caused. Concentration (ϕ) is markedly increased, in particular at some distance from the sphere surface, with an increase in Forchheimer parameter, Λ. As with temperature response, the concentration profiles exhibit a monotonic decay from the sphere surface to the edge of the boundary layer regime.

Fig. 6(a)–6(c) depicts the velocity (f'), temperature (θ) and concentration (ϕ) distributions for various values of Darcy parameter, Da. Velocity is clearly enhanced considerably with increasing Darcy number as shown in Fig. 6(a), since greater permeability of the regime corresponds to a decrease in Darcian drag force. The velocity peaks close to the sphere surface are also found to be displaced further from the wall with increasing Darcy number. A very strong decrease in temperature (θ) and concentration (ϕ), as shown in Figs. 6(b) and 6(c) respectively, occurs with increasing Da values. The progressive reduction in solid fibers in the porous medium with large Da values serves to decrease thermal conduction heat transfer in the regime. This inhibits the diffusion of thermal energy from the sphere surface to the regime and cools the boundary layer also decreasing thermal boundary layer thickness. Concentration boundary layer thickness will also be decreased with a rise in Darcy number.

Fig. 7(a)–7(c) presents typical profiles for velocity (f'), temperature (θ) and concentration (ϕ) for various values of the conduction-radiation parameter, F. Increasing F strongly decelerates the flow i.e. decreases velocity. This parameter features in the term, $\frac{1}{Pr}\left(1+\frac{4}{3F}\right)\theta''$ in the energy conservation Eq. (14). $F = \frac{Kk^*}{4\sigma^* T_\infty^3}$ represents the relative contribution of *thermal conduction* to *thermal radiation* heat transfer. For $F = 1$ both modes of heat transfer have the same contribution. For $F > 1$ *thermal conduction* dominates over *thermal radiation flux*. *For* $F < 1$ thermal radiation contributes more than thermal conduction. The first two of these three cases are considered here. The decreasing contribution of thermal radiation with an increase in F values depletes the thermal diffusivity of the fluid regime and reduces thermal energy in the boundary layer. Temperatures are therefore also decreased, as observed in Fig. 7(b). Both momentum and thermal boundary layer thicknesses are reduced with a decreasing contribution from thermal radiation i.e. with increasing thermal conduction contribution (large F values). Conversely there is a slight enhancement in concentration values with increasing F values, as shown in Fig. 7(c).

Fig. 8(a)–8(c) presents typical profiles for velocity (f'), temperature (θ) and concentration (ϕ) for various values of heat generation or absorption parameter, Δ. Increasing heat generation ($\Delta > 0$) significantly accelerates the flow and also increases temperature magnitudes but reduces concentration values. The present of a progressively stronger heat source is therefore beneficial to the regime. Conversely with a heat sink present, ($\Delta < 0$) the flow is retarded (momentum boundary layer thickness is lowered), thermal boundary layer thickness is reduced whereas the concentration boundary layer thickness increases.

Fig. 9(a)–9(c) shows the influence of Deborah number, De on dimensionless skin friction coefficient ($\xi f''(\xi,0)$), heat transfer rate ($\theta'(\xi,0)$) and mass transfer rate ($\phi'(\xi,0)$) at the sphere surface. It is observed that the dimensionless skin friction is decreased with the increase in the Deborah number, De i.e. the boundary layer flow is decelerated with *greater elasticity effects* in the non-Newtonian fluid. Likewise on the other hand the heat transfer rate is also substantially decreased with increasing De values. There is also a progressive decay in heat transfer rate (local Nusselt number) with increasing tangential coordinate i.e. ξ-value. A decrease in heat transfer rate at the wall will imply less heat is convected from the fluid regime to the sphere, thereby heating the boundary layer. The mass transfer rate (local Sherwood number) is also found to be suppressed with increasing values of De and furthermore plummets with further distance from the lower stagnation point (i.e. higher ξ values).

Fig. 10(a)–10(c) illustrates the response to the parameter ratio of relaxation and retardation times, λ, on the dimensionless skin friction coefficient ($\xi f''(\xi,0)$), heat transfer rate ($\theta'(\xi,0)$) and mass transfer rate ($\phi'(\xi,0)$) at the sphere surface. The skin friction at the sphere surface is accentuated with increasing λ. Also there is a strong elevation in shear stress (skin friction coefficient) with increasing value of the tangential coordinate, ξ. The flow is therefore strongly accelerated along the curved sphere surface away from the lower stagnation point. Heat (local Nusselt number) and mass transfer (local Sherwood number) rates are increased with increasing, λ., *although not as profoundly as the skin friction*. With increasing values of the tangential coordinate, ξ, however both local

Nusselt number and local Sherwood number are depressed. As elaborated earlier these characteristics are only maximized at the lower stagnation point.

Fig. 11(a)–11(c) presents the influence of the radiation parameter, F, on the dimensionless skin friction coefficient $(\xi f''(\xi,0))$, heat transfer rate $(\theta'(\xi,0))$ and mass transfer rate $(\phi'(\xi,0))$ at the sphere surface. The skin friction at the sphere surface is found to be decreasing with increasing F i.e. with decreasing thermal radiative flux magnitudes (stronger thermal conduction effect). Local Nusselt number (surface heat transfer rate) is conversely observed to be strongly increased with increasing F values. Stronger thermal radiation therefore accelerates the flow but reduces heat transfer to the sphere surface. Local Sherwood number (mass transfer rate) is considerably reduced with increasing F values. The greater contribution of thermal conduction heat transfer (and lower radiative contribution) inhibits species diffusion to the sphere surface. Skin friction is also enhanced with greater distance along the curved surface i.e. with increasing ξ values whereas both local Nusselt and Sherwood numbers are decreased. Overall the strong effect of thermal radiation in porous media transport of viscoelastic fluids is clearly observed.

6. Conclusions

Numerical solutions have been presented for the buoyancy-driven heat and mass transfer in radiative Jeffreys flow external to an isothermal sphere, in a porous medium with heat source/sink effects. The Keller-box implicit second order accurate finite difference numerical scheme has been utilized to efficiently solve the transformed, dimensionless velocity, thermal and concentration boundary layer equations, subject to realistic boundary conditions. The results so obtained are in good correlation with those obtained by Huang and Chen [55] as shown in Table 4. The computations have shown that:

(1) Increasing the Deborah number (De) reduces the velocity, skin friction, local Nusselt number and local Sherwood number whereas it enhances temperature and concentration boundary layer thicknesses.
(2) Increasing the parameter ratio of relaxation and retardation times (λ), increases velocity, skin friction coefficient, local Nusselt number and local Sherwood number whereas it decreases the temperature and concentration for all values of radial coordinate.
(3) Increasing Forchheimer parameter, Λ, decelerates the flow whereas it elevates both temperature and concentration magnitudes.
(4) Increasing the conduction-radiation parameter, F, depresses velocity, skin friction, local Sherwood number and temperature (due to a reduction in radiative heat transfer flux contribution compared with enhanced thermal conduction contribution) but enhances concentration and local Nusselt number.
(5) Increasing heat generation, $(\Delta > 0)$, accelerates the flow and temperature throughout the boundary layer regime but depresses the concentration, with the opposite effect computed for increasing heat absorption $(\Delta < 0)$.

The present study has considered the Jeffreys viscoelastic model and demonstrated the excellent stability and convergence characteristics of the Keller – Box numerical scheme. Future studies will investigate transport phenomena in porous media using alternative non-Newtonian models e.g. Maxwell fluids [54] and will be communicated imminently.

References

[1] Hyder JL, Garrett PM. A theoretical model for *in situ* leaching of radionuclides from buried radioactive waste. Nucl Chem Waste Manage 1982;3:149–52.
[2] Bechthold W, Smailos E, Heusermann S, Bollingerfehr W, Bazargan-Sabet B, Rothfuchs T, et al. Backfilling and sealing of underground repositories for radioactive waste in salt (BAMBUS-II Project). Final report EUR 20621 EN. Luxembourg: Office for Official Publications of the European Community. ERMS 534716; 2004.
[3] Reda DC. Natural convection experiments with a finite-length, vertical, cylindrical heat source in a water-saturated porous medium. Nucl Chem Waste Manage 1986;6:3–14.
[4] Anwar Bég O, Makinde OD. Viscoelastic flow and species transfer in a Darcian high-permeability channel. J Petrol Sci Eng 2011;76:93–9.
[5] Hayat T, Shehzad SA, Qasim M, Obaidat S. Radiative flow of Jeffreys fluid in a porous medium with power law heat flux and heat source. Nucl Eng Des 2012;243:15–9.
[6] Tingey JM, Bredt PR, Shekarriz R. Rheology and settling behavior of hanford tank wastes and the resulting process streams. In: Rheology in mineral industry II-conference, Kahuku, Oahu, Hawaii, USA; 1999.
[7] Sochi T. Non-Newtonian flow in porous media. Polymer 2010;51:5007–23.
[8] Kozicki W. Viscoelastic flow in packed beds or porous media. Can J Chem Eng 2001;79:124–31.
[9] Kadet VV, Polonskii DG. Law of flow of a viscoplastic fluid through a porous medium with allowance for inertial losses. Fluid Dyn 1999;34:58–63.
[10] López De Haro M, Del Río JAP, Whitaker S. Flow of Maxwell fluids in porous media. Transp Porous Media 1996;25:167–92.
[11] Rao BK. Internal heat transfer to power-law fluid flows through porous media. Exp Heat Transfer 2002;15:73–87.
[12] Sorbie KS, Clifford PJ, Jones ERW. The rheology of pseudoplastic fluids in porous media using network modeling. J Colloid Interface Sci 1989;130:508–34.
[13] Tripathi D, Anwar Bég O. Magnetohydrodynamic peristaltic flow of a couple stress fluid through coaxial channels containing a porous medium. J Mech Med Biol 2012;12(5):1250088.1–88.2.
[14] Rashidi MM, Anwar Bég O, Rastegari MT. A study of non-Newtonian flow and heat transfer over a non-isothermal wedge using the homotopy analysis method. Chem Eng Commun 2012;199(2):231–56.
[15] Vafai K. Convective flow and heat transfer in variable-porosity media. J Fluid Mech 1984;147:233–59.
[16] Anwar Bég O, Bhargava R, Rawat S, Kahya E. Numerical study of micropolar convective heat and mass transfer in a non-Darcian porous regime with Soret/Dufour diffusion effects. Emirates J Eng Res 2008;13(2):51–66.
[17] Kairi RR, Murthy PVSN. Effect of melting on mixed convection heat and mass transfer in a non-Newtonian fluid saturated non-Darcy porous medium. ASME J Heat Transf 2012;134:042601–8.
[18] Anwar Bég O, Zueco J, Ghosh SK. Unsteady hydromagnetic natural convection of a short-memory viscoelastic fluid in a non-Darcian regime: network simulation. Chem Eng Commun 2010;198:172–90.

[19] Prasad KV, Abel MS, Khan SK, Datti PS. Non-Darcy forced convective heat transfer in a viscoelastic fluid flow over a non-isothermal stretching sheet. J Porous Media 2002;5:80–7.
[20] Rashidi MM, Keimanesh M, Anwar Bég O, Hung TK. Magneto-hydrodynamic biorheological transport phenomena in a porous medium: a simulation of magnetic blood flow control and filtration. Int J Numer Methods Biomed Eng 2011;27:805–21.
[21] Bhatnagar RK. On heat transfer in a viscoelastic fluid flowing around a steadily rotating and thermally insulated sphere. Rheol Acta 1970;9(3):419–23.
[22] Lee TL, Donatelli AA. Mass transfer by natural convection from a solid sphere to power law fluids. Ind Eng Chem Res 1989;28:105–7.
[23] Nazar R, Amin N, Pop I. Free convection boundary layer on an isothermal horizontal circular cylinder in a micropolar fluid. In: Proc 12th int heat transfer conference, Grenoble, France; August 18–23, 2002.
[24] Dhole SD, Chhabra RP, Eswaran V. Forced convection heat transfer from a sphere to non-Newtonian power law fluids. AIChE J 2006;52:3658–67.
[25] Prasad VR, SubbaRao A, Bhaskar Reddy N, Vasu B, Anwar Bég O. Modelling laminar transport phenomena in a Casson rheological fluid from a horizontal circular cylinder with partial slip. Proc IMechE – Part E: J Process Mech Eng 2012. http://dx.doi.org/10.1177/0954408912466350.
[26] Anwar Bég O, Prasad VR, Vasu B, Bhaskar Reddy N, Li Q, Bhargava R. Free convection heat and mass transfer from an isothermal sphere to a micropolar regime with Soret/Dufour effects. Int J Heat Mass Transf 2011;54:9–18.
[27] Akbar Noreen Sher, Khan Zafar Hayat, Nadeem S. The combined effects of slip and convective boundary conditions on stagnation-point flow of CNT suspended nanofluid over a stretching sheet. J Mol Liq 2014;196:21–5.
[28] Rudraiah N, Sasikumar TP. Radiation and non-Darcy effects on convection in porous media. Chem Eng Commun 1990;87:53–65.
[29] Talukdar P, Mishra SC, Trimis D, Durst F. Combined radiation and convection heat transfer in a porous channel bounded by isothermal parallel plates. Int J Heat Mass Transf 2004;47:1001–13.
[30] Yih K-A. Radiation effect on mixed convection over an isothermal wedge in porous media: the entire regime. Heat Transfer Eng 2001;22:26–32.
[31] Takhar HS, Anwar Bég O, Kumari M. Computational analysis of coupled radiation convection dissipative flow in a porous medium using the Keller-box implicit difference scheme. Int J Energy Res 1998;22:141–59.
[32] Hayat T, Alsaedi A, Shehzad SA. Three dimensional flow of Jeffreys fluid with convective surface boundary conditions. Int J Heat Mass Transf 2012;55:3971–6.
[33] Akbar Noreen Sher. Double-diffusive natural convective peristaltic flow of a Jeffrey nanofluid in a porous channel. Heat Transf Res 2014;45(4):293–307. http://dx.doi.org/10.1615/HeatTransRes.2013006995.
[34] Sher Akbar Noreen, Nadeem S, Noor M. Free convective MHD peristaltic flow of a Jeffrey nanofluid with convective surface boundary condition: a biomedicine-Nano model. Current Nano Sci 2014;10(3):432–40 (9).
[35] Akbar Noreen Sher, Nadeem S. Analytical and numerical study of peristaltic transport of a Johnson-Segalman fluid in an endoscope. Chin Phys B 2013;22(1):014703. http://dx.doi.org/10.1088/1674-1056/22/1/014703.
[36] Akbar Noreen Sher, Nadeem S. Mixed convective magnetohydrodynamic peristaltic flow of a Jeffrey nanofluid with Newtonian heating. Z Naturforsch A 2013;68a:433–41. http://dx.doi.org/10.5560/ZNA.2013-0029.
[37] Lanza F, Parnisari E. Influence of film formation and its composition on the leaching of borosilicate glasses. Nucl Chem Waste Manage 1981;2:131–7.
[38] Bird RB, Armstrong RC, Hassager O. Dynamics of polymeric liquids. Fluid mechanics, vol. 1. New York (USA): Wiley; 1977.
[39] Gorla RSR. Radiative effect on conjugate forced convection in a laminar wall jet along a flat plate, suppl. 3: advances in flows dynamics. Texas (USA): Gulf Publishing; 1993.
[40] Anwar Bég O, Zueco J, Ghosh SK, Heidari A. Unsteady magnetohydrodynamic heat transfer in a semi-infinite porous medium with thermal radiation flux: analytical and numerical study. Adv Numer Anal 2011;2011:1–17.
[41] Keller HB. Numerical methods in boundary-layer theory. Ann Rev Fluid Mech 1978;10:417–33.
[42] Rossi C, Rouhani MD, Esteve D. Prediction of the performance of a Si-micro-machined microthruster by computing the subsonic gas flow inside the thrusters. Sensors Actuators 2000;87:96–104.
[43] Sturdza P. An aerodynamic design method for supersonic natural laminar flow aircraft. PhD thesis. California (USA): Dept. Aeronautics and Astronautics, Stanford University; December, 2003.
[44] Croisille J-P. Keller's box-scheme for the one-dimensional stationary convection-diffusion equation. Computing 2002;68(1):37–63.
[45] Prasad VR, Vasu B, Anwar Bég O. Thermo-diffusion and diffusion-thermo effects on MHD free convection flow past a vertical porous plate embedded in a non-Darcian porous medium. Chem Eng J 2011;173:598–606.
[46] Narayana M, Sibanda P, Motsa SS, Siddheshwar PG. On double-diffusive convection and cross diffusion effects on a horizontal wavy surface in a porous medium. Boundary Value Problems 2012;88:1–22.
[47] Anwar MI, Khan I, Sharidan S, Salleh MZ. Conjugate effects of heat and mass transfer of nanofluids over a nonlinear stretching sheet. Int J Phys Sci 2012;7:4081–92.
[48] Shu J-J, Wilks G. Heat transfer in the flow of a cold, two-dimensional draining sheet over a hot, horizontal cylinder. Eur J Mech B/Fluids 2007;26:1–5.
[49] Ali FM, Nazar R, Arifin NM, Pop I. Unsteady shrinking sheet with mass transfer in a rotating fluid. Int J Numer Methods Fluids 2011;66:1465–74.
[50] Kaya A. Heat and mass transfer from a horizontal slender cylinder with a magnetic field effect. Therm Sci Technol 2011;31(2):73–8.
[51] Kumar BVR, Murthy SVK. Soret and Dufour effects on double-diffusive free convection from a corrugated vertical surface in a non-Darcy porous medium. Transp Porous Media 2010;85:117–30.
[52] Esfahanian V, Torabi F. Numerical simulation of lead–acid batteries using Keller–box method. In: Lead-acid batteries (LABAT) conference, Sofia, Bulgaria; 2005.
[53] Kaviany M. Principles of heat transfer in porous media. New York (USA): MacGraw-Hill; 1992.
[54] Tripathi D, Anwar Bég O. A numerical study of oscillating peristaltic flow of generalized Maxwell viscoelastic fluids through a porous medium. Transp Porous Media 2012. http://dx.doi.org/10.1007/s11242-012-0046-5.
[55] Huang MJ, Chen CK. Laminar free-convection from a sphere with blowing and suction. J Heat Mass Transf 1987;109:529–32.

S. Abdul gaffar was born in Madanapalle, Chittoor District, Andhra Pradesh, India in May, 1982. He obtained a First Class Masters of Sciences, degree in Mathematics (2004) from Sri Venkateswara University, Tirupathi and is persuing PhD in Flow and Heat transfer of Casson Fluid on Boundary Layer (Registerd in 2011), JNT University Anantapuramu, Anantapur. He worked as lecturer in the Department of Mathematics, Bapatla College of Engineering, India for one year (2004). Later from May 2007 to April 2013, he was the Assistant Professor for five years in the Department of Mathematics, Mother Theresa Institutions. From 2013 to till date he is working as Lecture in the Department of Mathematics, Salalah college of Technology, Salalah, OMAN. He has published in excess of 12 journals in peer reviewed journals. He is currently engaged in different non-Newtonian fluids over different curved bodies.

Professor **Dr. V. Ramachandra Prasad** was born in Madanapalle, Chittoor District, Andhra Pradesh, India in July, 1968. He obtained a Distinction Class Masters of Sciences, degree in Mathematics (1994) from Osmania University, Hyderabad and a PhD in Radiation and Mass Transfer Effects on connective flow past a vertical plate (2003), both from Sri Venkateswara University, Tirupathi. He then worked as lecturer in the Department of Mathematics, Besant Theosophical College, Madanapalle, India for seven years (1994-2001). From May 2001 to April 2007, he was the Assistant Professor for six years in the Department of Mathematics, in Madanapalle Institute of Technology and Science. Later from May 2007 to April 2009 worked as Associate Professor, in the Department of Mathematics, Madanapalle Institute of Technology and Science, Madanapalle, India. Form May 2009 to till date he is working as Professor in the Department of Mathematics, Madanapalle Institute of Technology and Science, Madanapalle, India. He has authored Radiation effects on Convective Flow Past a Vertical Palte: Radiation and Mass Transfer Effects on Convective Flow Past a Vertical Plate, (*Lambert, Germany, 2010*), *Thermo-Diffusion and Diffusion-Thermo Effects on Boundary Layer Flows* (*Lambert, Germany, 2011*) *and Walters_B Viscoelastic flow Past a Vertical Plate: Numerical Study of Unsteady Free Convective Heat and Mass Transfer in a Walters_B Viscoelastic Flow Past a Vertical Plate* (*Lambert, Germany, 2012*). He has published in excess of 50 journal articles. His research has also been presented at over 13 conferences. He is currently engaged in different non-Newtonian fluids over different curved bodies.

Dr. E. Keshava Reddy, presently working as Professor of Mathematics in JNT University College of Engineering Anantapur. He has 15 years of experience in teaching and 11 years in research. He obtained his Ph.D. degree in Mathematics from prestigious University Banaras Hindu University varanasi. His areas of interest include Functional Analysis, Optimization Techniques, Data Mining, Neural Networks, Fuzzy Logic and Optimization technics. He guided 2 Ph.D., 1 M.Phil and has published more than 35 Research papers in National and International Journals and Conferences. He authored 06 books on Engineering Mathematics and Mathematical Methods for various universities. He worked as Chairman of Board of studies for the faculty of Mathematics for JNTUA both at UG level and PG level. Presently he is the chairman, PG Board of studies for Mathematics of JNTUA. He is a member of Board of Studies for Mathematics of various universities.

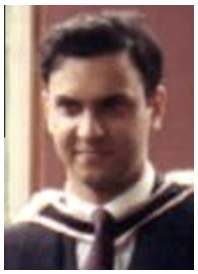

Professor **Dr. O. Anwar Bég** was born in Dewsbury, Yorkshire, England in September, 1969. He obtained a First Class BEng (Hons) degree in Engineering (1992) and a PhD in Computational Magnetohydrodynamics (1996), both from the University of Manchester. He then worked in automotive, aerospace, structural, geotechnical, earthquake dynamics, ocean and fire safety engineering analysis for five years (1996-2001) where he was involved with aero-structural analysis/dynamics, fluid flow modeling, bridge dynamics and geomechanics. He attended the *First MIT Conference in Computational Fluid and Solid Mechanics, was Course Director of the BSc (Hons) in Fire Safety Engineering Sciences at Leeds Metropolitan University* from February 2002 to April 2007, where he also taught human dynamics, structural mechanics, applied mathematics, fire dynamics, explosion sciences, thermofluids and acoustics. He then taught aerodynamics at *BAE Systems, Riyadh, Arabia* and researched hypersonic flows. From Sep/ 2007 to Sep. 2012, he was the Associate Professor and Director of the *MEng (Hons) degree in Aerospace Engineering at Sheffield Hallam University*. Since September 2012 he has been Visiting Professor in Norway, France, Germany and Indonesia and has worked as an Aerospace and Medical Consultant with many companies in Europe and the USA in *supersonic and hypersonic aerodynamics, marine propulsion, ice engineering, computational nano-solid mechanics and geological systems*. He has also authored *Giants of Engineering Science* (*Matador, UK, 2003*) and co-authored *Applied Magnetofluid Dynamics: Modelling and Computation* (*Lambert, Germany, 2011*) and *Numerical Simulation in Micropolar Fluid Dynamics* (*Lambert, Germany, 2011*). He has published in excess of 300 journal articles, ten book chapters and many editorials and in many leading journals including *ZAMP (Switzerland), Computational Materials Science (Germany), Physica Scripta (Sweden), AIAA J. Thermophysics & Heat Transfer (USA), Computers and Mathematics with Applications USA, Mathematical Biosciences (USA), Brazilian J. Mechanical Sciences and Engineering, Advanced Materials Research (Italy), J. Magnetism and Magnetic Materials (USA), Applied Nanoscience (Arabia/Germany, Springer), J. Nanofluids (USA), Applied Bionics and Biomechanics (Netherlands), Steel and Composite Structures (Korea/USA)*. His research has also been presented at over 30 conferences, including work on finite element damage mechanics at the *European Congress on Computational Methods in Applied Sciences and Engineering* (*ECCOMAS 2012*), *Vienna, Austria, September* (*2012*). He is currently engaged in 3-D simulations of curved tube peristaltic propulsion, hydroelasticity, thermal consolidation mechanics and electro-pneumatic modelling. In 2013 he was awarded an honorary DSc (Eng) degree for his contributions to theoretical and computational magnetohydrodynamics in engineering propulsion and energy systems. He has been an *Associate Editor* of the *Journal of Mechanics in Medicine and Biology* since 2010. He is affiliated with ASCE, ASME, AIAA, SES (USA), IAHR (Holland) and SIAM (USA). His hero in science is L.D. Landau, pioneer in superfluidity and superconductivity.